

Indian Head Division
Naval Surface Warfare Center
Indian Head, MD 20640-5035

IHTR 2058
24 December 1997

COMPUTATION OF PRESSURES OF LINEAR CHARGE ARRAYS USING RAY TRACING TECHNIQUES

William W. McDonald

Approved for public release; distribution is unlimited.

19980811 029



REPORT DOCUMENTATION PAGE			Form Approved QMB No. 0704-0188	
Public reporting burden for this collection of information is estimated to average 1 hour per response, including the time for reviewing instructions, searching existing data sources, gathering and maintaining the data needed, and completing and reviewing the collection of information. Send comments regarding the burden estimate or any other aspect of this collection of information, including suggestion for reducing this burden, to Washington Headquarters Services, Directorate for Information Operations and Reports, 1215 Jefferson Davis Highway, Suite 1204, Arlington, VA 22202-4302, and to the Office of Management and Budget, Paperwork Reduction project (0704-0188), Washington, DC 20503.				
1. AGENCY USE ONLY (Leave Blank)	2. REPORT DATE 24 December 1997	3. REPORT TYPE AND DATES COVERED Final Report		
4. TITLE AND SUBTITLE COMPUTATION OF PRESSURES OF LINEAR CHARGE ARRAYS USING RAY TRACING TECHNIQUES			5. FUNDING NUMBERS	
6. AUTHOR(S) William W. McDonald				
7. PERFORMING ORGANIZATIONS NAME(S) AND ADDRESS(ES) Indian Head Division Naval Surface Warfare Center Indian Head, MD 20640-5035			8. PERFORMING ORGANIZATION REPORT NUMBER IHTR 2058	
9. SPONSORING/MONITORING AGENCY NAME(S) AND ADDRESS(ES) Office of Naval Research Arlington, VA 22217-5000			10. SPONSORING/MONITORING AGENCY REPORT NUMBER	
11. SUPPLEMENTARY NOTES				
12a. DISTRIBUTION/AVAILABILITY STATEMENT Approved for public release; distribution is unlimited.			12b. DISTRIBUTION CODE	
13. ABSTRACT (Maximum 200 words) Classical ray tracing techniques based upon acoustic theory are shown to effectively reproduce pressures measured in tests of linear arrays of bulk charges placed near a sand bottom. It is shown that accurate agreement with measured records rests upon the determination of a bottom reflection coefficient as a function of the problem geometry and other problem-dependent conditions. In the present model, bottom reflection coefficient functions suitable for modeling the results of 1995 Eglin AFB tests are determined empirically. Consequently, the model is not currently suitable for predicting pressures at other test sites.				
14. SUBJECT TERMS Underwater explosions Pressure modeling Multiple charges			15. NUMBER OF PAGES 57	
Ray tracing Acoustic theory			16. PRICE CODE	
17. SECURITY CLASSIFICATION OF REPORT UNCLASSIFIED	18. SECURITY CLASSIFICATION OF THIS PAGE UNCLASSIFIED	19. SECURITY CLASSIFICATION OF ABSTRACT UNCLASSIFIED	20. LIMITATION OF ABSTRACT SAR	

FOREWORD

This work was sponsored by the Office of Naval Research (Code 3210E, Dr. Thomas Swean).

Approved by:

J.B. Almquist

Brian Almquist
Director, Warhead Performance and Lethality Division

Released by:

Wm Hinckley

William M. Hinckley
Head, Underwater Warheads Technology
and Development Department

This page intentionally left blank.

CONTENTS

<i>Heading</i>	<i>Page</i>
Foreword	iii
Introduction	1
Model Development	2
Discussion of Model Performance	7
Model Calibration	11
Comparison of Constant Φ Model Calculations with Measurements in Water 10 Feet Deep	12
Comparison of Constant Φ Model Calculations with Measurements in Water 3 Feet Deep	20
Model Consistency and Measurement Reproducibility	27
Development of the Variable Φ Model	29
Conclusions	33
References	34
Appendix A. Comparison of Variable Φ Model Calculations with Measurements	A-1

Tables

I. Conditions and Figure Numbers of Analyzed 1995 Eglin Tests	11
---	----

Figures

1. Line Charge Geometry	2
2. Ray Geometries	3
3. Calculated Pressure-Time Curve	7
4. Comparison with Measurements	8
5. Leading Pulses	9
6. Comparison of Averaged Pulses with Measurements	9
7. D-Sabre Wave Fronts	10
8. M58 and C-Sabre Wave Fronts	10
9. Calculated Impulse-Time Curve	10
10. Results of M58 Shot 4286	13
11. Results of D-Sabre Shot 4287	16
12. Results for C-Sabre Shot 4288	18
13. Results for M58 Shot 4283	21
14. Results of D-Sabre Shot 4284	23
15. Results for C-Sabre Shot 4285	25
16. Comparison of Identical Gage Position Results for D-Sabre Shots 4284 (Left) and 4287 (Right)	27
17. M58 Reflection Coefficients Versus Angle	30
18. D-Sabre Reflection Coefficients Versus Angle	31
19. C-Sabre Reflection Coefficients Versus Angle	32

This page intentionally left blank.

INTRODUCTION

In this report we describe a model to predict the pressure field developed in shallow water by a linear array of equally spaced, discrete explosive charges placed near a sand bottom. The method, suggested to the author by Gaspin,¹ has a theoretical foundation that rests on the works of Arons and Yennie,² Rosenbaum,³ Cagniard et al.,⁴ Snay,^{5,6} and Britt,^{6,7,8} who treated in considerable detail the pressure field produced by a single underwater charge in the presence of free surface and bottom interfaces.

Presently, the pressure field model is an empirical model based upon data from the Eglin Air Force Base test site. This enables the model to be used to reliably predict the pressures associated with mine vulnerability tests conducted at Eglin,¹ but the model has not been validated for other venues. The model is capable of extension to other locations by making use of the physical theory cited above, principally that developed by Britt and Snay. The necessary physics, however, has not been built into the current, interim model.

The intention of this modeling effort was to produce a computationally efficient code that would describe the pressure histories at arbitrary field locations to levels of accuracy adequate for nondeterministically modeling Eglin mine response data. The quasi-impulsive nature of the mine kill response mechanism, which integrates the finer details of the pressure pulse signature, and the presence of random scatter in the mine kill data suggested that an adequate mine kill prediction model could be fashioned using approximate classical modeling techniques. The primary modeling objective was to predict mine kill probability as a function of variables that were systematically controlled in the tests with enough of the underlying physics included to permit extrapolation and interpolation of the model to untested conditions.

Given the caveat of site dependency, the model presented below will be shown to possess "accuracy" by various measures that is perhaps surprising in view of the model simplicity. Comparisons are made with gage pressure histories at all interesting in-water gage positions used in the 1995 Eglin tests. Eglin pressure histories obtained at gage positions 2 inches above the sand-water interface are used to calibrate the model and to confirm the basic physical process by which line charge pressures arise.

MODEL DEVELOPMENT

Let the origin of a right-hand coordinate system be on the water surface with the z axis positive downward and the x and y axes as illustrated in Figure 1. We consider a linear array of bulk charges lying in the $y = 0$ plane parallel to the x axis at a depth d_a . Let the first charge be located at $x = 0$ with the remaining N charges extending in the positive x direction at spacings of Δx_{chg} . Thus, for $i := 1 \dots N$, the i th charge has coordinates

$$x_{c_i} := (i - 1) \cdot \Delta x_{\text{chg}}, \quad y_{c_i} := 0, \quad \text{and} \quad z_{c_i} := d_a. \quad (1)$$

Assuming detonation of the charge at the origin first, the detonation time of the i th charge is

$$t_{\text{det}_i} := t_0 + \frac{(i - 1) \cdot \Delta x_{\text{det}}}{v_{\text{det}}} \quad (2)$$

where t_0 is the temporal origin, here taken as zero, Δx_{det} is the length of the detonating cord between charges, and v_{det} is the speed of the detonation wave along the detonating cord.

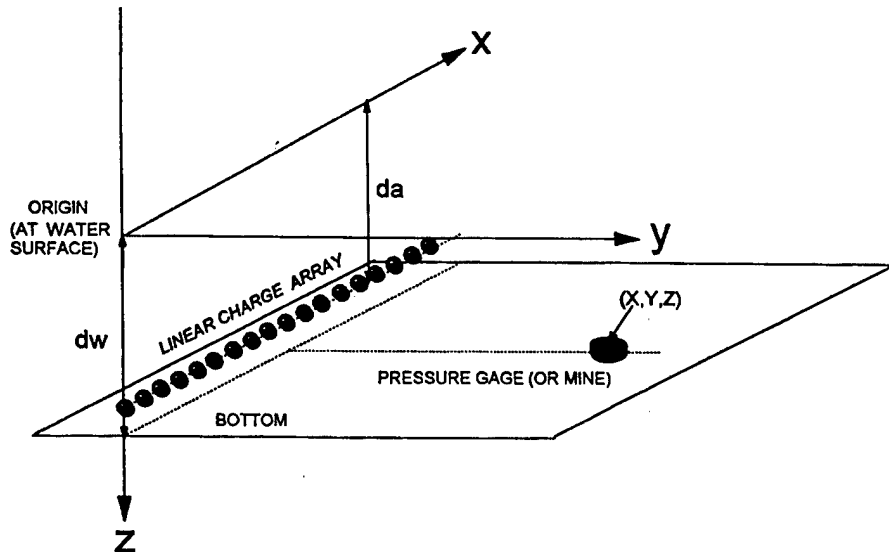


Figure 1. Line Charge Geometry

Let a pressure gage be located at a point with coordinates X, Y, Z . As described, e.g., by Britt and Snay,⁶ we will assume that the gage signal originating from each charge of the line charge array consists of three additive components: (1) a direct component, (2) a surface-reflected component, and (3) a bottom-reflected component. The two reflected components will be modeled using image charges as shown in Figure 2. We will assume that the complete pressure history produced by the line charge array at this gage position can be represented by additively combining, at each time of interest, these three components for all charges of the array.

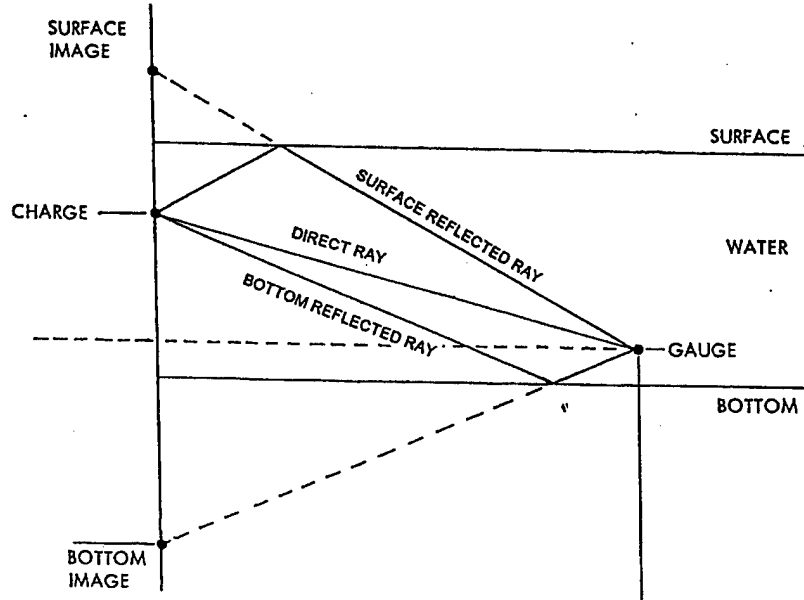


Figure 2. Ray Geometries

The location of the surface-reflected image of the i th charge is given by coordinates

$$x_{s_i} := x_{c_i}, \quad y_{s_i} := y_{c_i}, \quad \text{and} \quad z_{s_i} := z_{c_i} \quad (3)$$

while those of the bottom-reflected image are given by

$$x_{b_i} := x_{c_i}, \quad y_{b_i} := y_{c_i}, \quad \text{and} \quad z_{b_i} := 2 \cdot d_w - z_{c_i} \quad (4)$$

Consequently, the direct line-of-sight slant range from the i th charge to the gage is

$$r_{d_i} := \sqrt{(X - x_{c_i})^2 + (Y - y_{c_i})^2 + (Z - z_{c_i})^2}, \quad (5)$$

that from the surface-reflected image of the i th charge is

$$r_{s_i} := \sqrt{(X-x_{s_i})^2 + (Y-y_{s_i})^2 + (Z-z_{s_i})^2}, \quad (6)$$

and that from the bottom-reflected image of the i th charge is

$$r_{b_i} := \sqrt{(X-x_{b_i})^2 + (Y-y_{b_i})^2 + (Z-z_{b_i})^2}. \quad (7)$$

Thus, the times of arrival at the gage of the direct, surface-reflected, and bottom-reflected signals from the i th charge are given by

$$t_{d_i} := t_{\text{det}_i} - \frac{r_{d_i}}{c}, \quad (8)$$

$$t_{s_i} := t_{\text{det}_i} + \frac{r_{s_i}}{c}, \quad (9)$$

and

$$t_{b_i} := t_{\text{det}_i} + \frac{r_{b_i}}{c}, \quad (10)$$

respectively, where c is the velocity of the shock waves. We shall use the acoustic approximation and assume c is equal to the water sound speed. For this we employ a formula published Snay and Kriebel⁵ and calculate c using the program

$$c = \left[\begin{array}{l} T - \frac{5}{9} \cdot (\text{Temp}_F - 32) \\ S - \text{Sal}_{\text{ppt}} \\ c_{\text{mps}} - 1449.3 + T \cdot (4.57191 - T \cdot (0.044524 + T \cdot (0.0002604 - T \cdot 0.0000079851))) \dots \\ \quad + (S - 35) \cdot (1.39807 + ((S - 35) \cdot 0.00169202 - T \cdot (0.011244 + T \cdot 0.00000077872))) \\ c_{\text{fps}} - \frac{c_{\text{mps}}}{0.3048} \end{array} \right] \quad (11)$$

which converts their formula from metric to English units and provides c in feet per second given water temperature in degrees Fahrenheit and salinity in parts per thousand.

We shall assume the direct, bottom-reflected, and surface-reflected shock waves from all charges to be spherical with exponential time dependence and overpressures of the form

$$P(r, t) \propto P_f(r) e^{-\frac{t-t_a}{\theta}}, \quad (12)$$

where $P_f(r)$ is the shock front overpressure at a distance r from the charge, θ is the decay constant, and t_a is the time of arrival at the gage. For directly arriving shocks the proportionality coefficient is taken to be unity. For reflected shocks, the proportionality coefficients will depend upon characteristics of the transporting and reflecting media.

The theory of surface-reflected waves (see Snay and Kriebel⁵) indicates that compression waves will become tension waves upon reflection from a free surface. Hence, the proportionality coefficient for surface-reflected waves will be negative in sign so that the amplitude of the reflected wave will be subtracted from the prevailing pressure that exists prior to the arrival of the surface-reflected pulse. Since water supports little pure tension, however, we shall not allow the absolute pressure to fall below zero. In this interim model we employ a proportionality coefficient of -1 for all surface-reflected waves. The theory indicates that this is an oversimplification, particularly for waves reflected at shallow angles. Eglin pressure measurements show, however, that gage pressures are strongly reduced upon arrival of the surface-reflected waves so that their strengths may be unimportant. Experience with the code suggests good agreement with pressure records is obtained with the -1 coefficient for gage positions near the sand-water interface. A more refined treatment of the surface-reflected waves may be necessary at other gage positions and for shallower water.

The theory of bottom-reflection is arguably more complicated than that for free surfaces. Britt has achieved remarkable success, however, in modeling shock wave reflections from complex, multi-layered bottom materials. His REFMS code relies principally on linear shock propagation theory, but recent enhancements of the code have extended it to highly nonlinear applications.⁸ Britt and Snay have suggested that reflections from materials that lack shear strength, such as sand, can be modeled using the simpler theory for non-rigid or "liquid" bottoms.⁶ The reflections of plane front shock waves from plane surfaces are often described by relationships like that of Equation 12 with coefficients of proportionality that are referred to as "reflection coefficients." We shall employ such a term in the present model and denote it as Φ . The reflection coefficient Φ can range in value from that appropriate for a free surface (-1) to that appropriate to a rigid surface ($+1$). The theory shows that Φ is a function of the reflection angle, the densities and wave speeds of the media, and also of time. Negative values may occur at small angles of reflection, even when the density and sound speed of the bottom material are greater than those of water. In this interim model we choose Φ empirically and represent it as a function of the reflection angle.

Using simple free field shock wave "similitude" equations (see, e.g., Cole,⁹ p. 235), we calculate shock front pressures for the i th charge at ranges corresponding to the direct, surface-reflected, and bottom-reflected waves as

$$P_{fd_i} := K_P \left[\frac{W^{\frac{1}{3}}}{r_{d_i}} \right]^{\alpha_P}, \quad P_{fs_i} := K_P \left[\frac{W^{\frac{1}{3}}}{r_{s_i}} \right]^{\alpha_P}, \quad \text{and} \quad P_{fb_i} := K_P \left[\frac{W^{\frac{1}{3}}}{r_{b_i}} \right]^{\alpha_P}, \quad (13)$$

respectively, where K_P and α_P are empirically determined coefficients that depend upon explosive type and W is the weight of the i th explosive charge. Similarly, time constants for the three component waves are represented by

$$\theta_{d_i} := K_\theta \cdot W^{\frac{1}{3}} \left[\frac{W^{\frac{1}{3}}}{r_{d_i}} \right]^{\alpha_\theta}, \quad \theta_{s_i} := K_\theta \cdot W^{\frac{1}{3}} \left[\frac{W^{\frac{1}{3}}}{r_{s_i}} \right]^{\alpha_\theta}, \quad \text{and} \quad \theta_{b_i} := K_\theta \cdot W^{\frac{1}{3}} \left[\frac{W^{\frac{1}{3}}}{r_{b_i}} \right]^{\alpha_\theta}. \quad (14)$$

Under the assumptions of the model, the pressure history at the gage at time t can be represented by the following function which, except for A and n , uses variables defined above. The quantity A is an ordered $n \times 3$ matrix, each row of which consists of a wave arrival time (column 1), the index of the charge from which the wave originated (column 0), and an index value equal to 0, 1, or 2 that identifies the row arrival time as a direct, bottom-reflected, or surface-reflected arrival (column 2) respectively. The rows of A are placed in order of ascending arrival times. Usually n is set to a value less than $3N$. To reduce calculation times, a truncation function is used to eliminate those rows in A after a specified number of surface-reflection arrivals. For example, in the figures shown in the next section the calculations were stopped after the arrival of 20 surface reflection pulses.

$$\begin{aligned}
 P(t, n, A, P_{fd}, P_{fb}, P_{fs}, \theta_d, \theta_b, \theta_s, t_d, t_b, t_s, \Phi) := & \left\{ \begin{array}{l} \text{sum} \leftarrow 14 \\ \text{for } j \in 1 \dots n-1 \\ \quad k \leftarrow (A^{<0>})_j \\ \quad \text{sum} \leftarrow \text{sum} + P_{fd_k} \cdot e^{-\frac{t-t_{d_k}}{\theta_{d_k}}} \text{ if } [(A^{<2>})_j = 0] \cdot [t \geq t_{d_k}] \\ \quad \text{sum} \leftarrow \text{sum} + \Phi \cdot P_{fb_k} \cdot e^{-\frac{t-t_{b_k}}{\theta_{b_k}}} \text{ if } [(A^{<2>})_j = 1] \cdot [t \geq t_{b_k}] \\ \quad \text{sum} \leftarrow \text{sum} - P_{fs_k} \cdot e^{-\frac{t-t_{s_k}}{\theta_{s_k}}} \text{ if } [(A^{<2>})_j = 2] \cdot [t \geq t_{s_k}] \\ \quad \text{sum} \leftarrow 0 \text{ if } \text{sum} < 0 \\ \text{sum} \end{array} \right. \quad (15)
 \end{aligned}$$

DISCUSSION OF MODEL PERFORMANCE

Figure 3 shows a pressure-time curve calculated using the model for an M58 line charge array as it was configured in the 1995 Eglin mine vulnerability tests. This linear array was composed of 198 2.5-pound C-4 charges spaced at 6-inch intervals. The center of each charge of the array was located 1.5 inches off the bottom in water 10 feet deep. The X , Y , and Z coordinates used in the calculation placed the gage along the perpendicular bisector of the array, 2 inches from the bottom, and at a standoff of 18 feet. For simplicity, a constant reflection coefficient value, $\Phi = -0.996$, was used rather than some more complicated function of reflection angle. This "constant Φ model" is compared with a "variable Φ model" later in this report.

The most prominent features of the calculated pressure-time curve are the pressure spikes and ramp buildup. Both features are due to the interplay between direct and bottom-reflected waves. The plus symbols shown along the top of the display are, from bottom to top, the arrival times of bottom-reflected shocks (brown), direct wave arrival times (blue), and the surface-reflected arrival times (red) respectively. Each pressure spike is caused by the arrival of a direct pulse followed almost immediately by a bottom-reflected tensile wave. As we shall see, the spikes have very short durations of about half a microsecond. Because of the Φ value, about 99.6% of the direct wave pressure amplitude is removed by the arrival of the bottom reflection. The ramp buildup is caused by the accumulation of the 0.4% residuals as more subtracting pairs reach the gage. Finally, the ramp is eliminated by the arrival of surface-reflected waves. Because of the short duration of the spikes, the ramp pressure is the primary source of the loading pressure on a target.

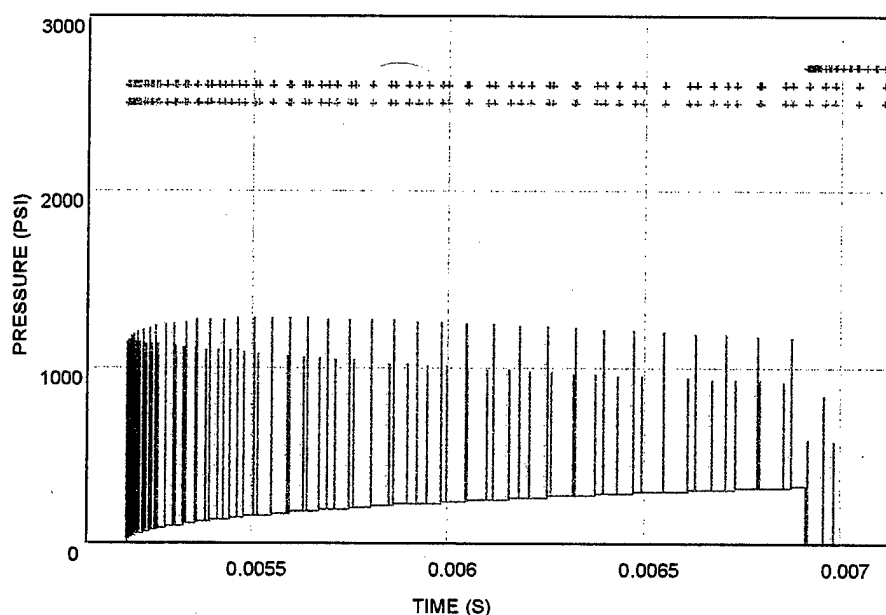


Figure 3. Calculated Pressure-Time Curve

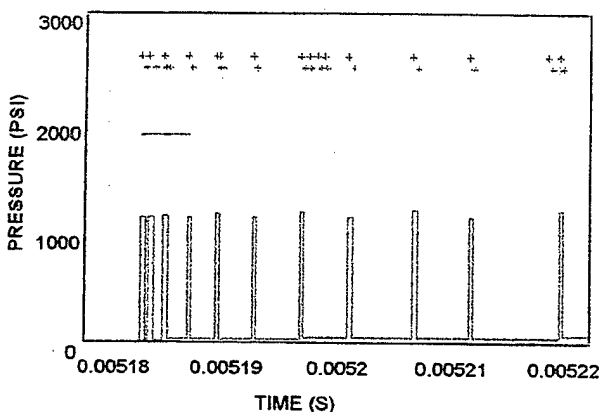


Figure 5. Leading Pulses

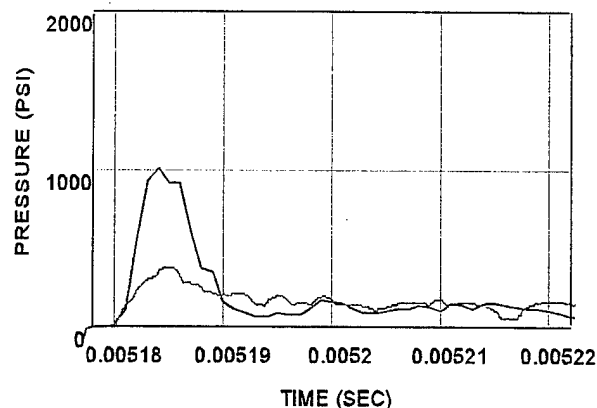


Figure 6. Comparison of Averaged Pulses with Measurements

To obtain the red curve of Figure 6, the pulses on the surface of the gage at each instant of time were numerically averaged. We assumed an "effective" gage diameter 50% larger than the actual diameter. The need for such a correction is well-known in the measurements community. This resulted in an approximately 90% reduction in the amplitude of the short duration spikes. While the amplitude of the leading pulse does not match the data, the spread of the leading pulse is in good agreement with measurements. Because the amplitudes of the calculated and measured pressures at later times are in excellent agreement, it appears reasonable to speculate that spikes such as those calculated may actually exist, but are not measurable in detail with the gages employed.

In their report on free surface reflections Snay and Kriebel suggested that for shock wave pressures of less than 10,000 psi and ray reflection angles of not less than 30 degrees, use of the acoustic approximation should result in a valid representation of the physics.⁵ The reflection angles encountered in shallow water for targets and line charges that rest on the bottom are much less than 30 degrees; hence, one might expect the approximation to fail under these conditions. Yet quite reasonable results have been obtained with the present model. Figures 7 and 8 illustrate wave front geometries 6 ms after detonation of the line charge systems of current interest. These depict graphically how the waves of particular charges run within the pressure fields of adjacent charges. For the M58 and continuous Sabre systems, shock front pressures drop below 10,000 psi at standoffs of about 3 feet, and for the larger discrete Sabre charges, the crossover occurs at about 4.7 feet. These distances, shown by dashed red lines in Figures 7 and 8, indicate that the acoustic wave speed assumption is a reasonable approximation throughout most of the region of interest defined more clearly below. This is also borne out by the agreement between the times of surface cutoff calculated and observed. Where the difference between shock and sound speeds may have significant effect is in regions where arrivals are densely packed, such as near the leading edge of the pulse train. It is suspected that the failure of the model to predict the initial peak, as well as other wave peak phenomena, may be due to such an effect.

In Figure 9 we compare the specific impulse of the calculated pressure pulse with that determined from the measured pressure-time data (again shifted by 65 μ s). Integration of the calculated pulse train includes the spikes, although because of the narrowness of the spike widths, the dominant contribution to the impulse derives from the ramp pressures. The close agreement suggests that the model would do well in predicting the response of quasi-impulsively driven systems. Details of the pressure history, such as the locations of spikes and other temporally local fluctuations, are of course less apparent in the integral curve.

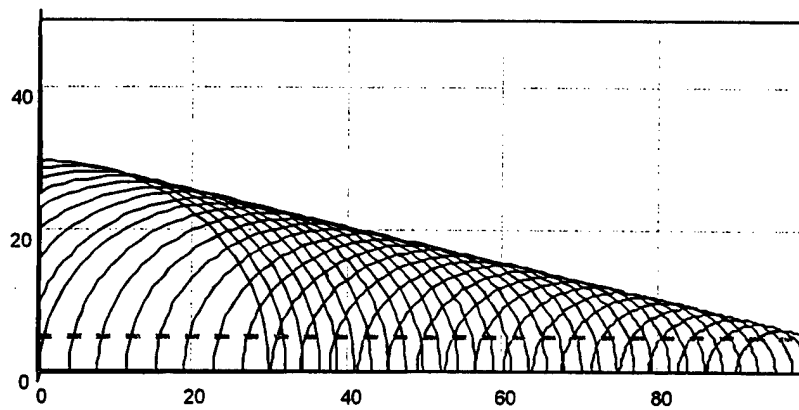


Figure 7. D-Sabre Wave Fronts

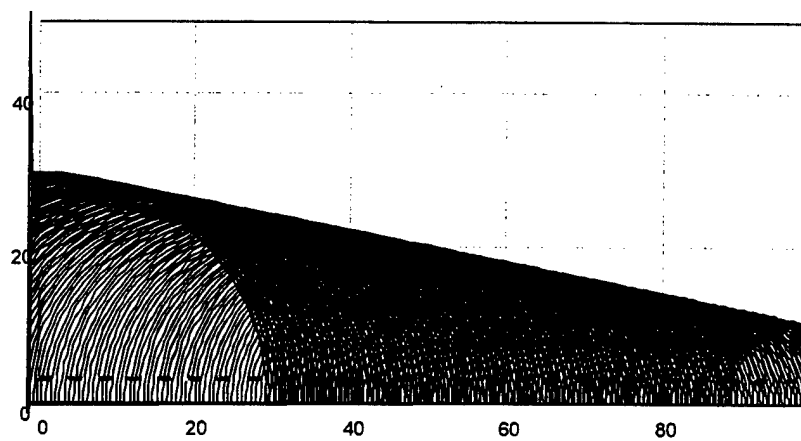


Figure 8. M58 and C-Sabre Wave Fronts

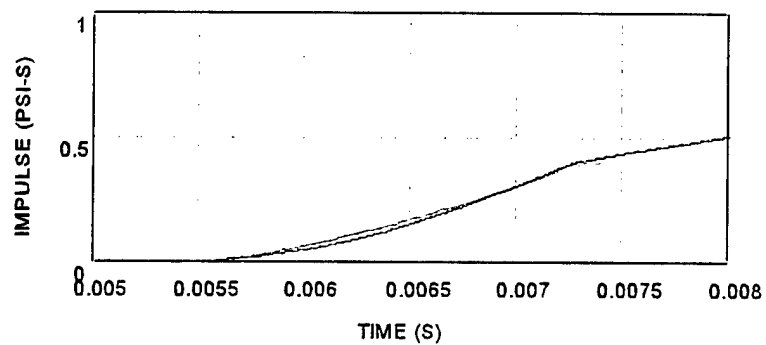


Figure 9. Calculated Impulse-Time Curve

MODEL CALIBRATION

In the above calculations, a constant reflection coefficient value was employed to calculate the strengths of the bottom-reflected waves from all charges of the array. Theory predicts, however, that Φ is not a simple constant, but a dependent variable that changes with time, the angle of reflection, and other conditions that may change from charge to charge, gage to gage, and one problem scenario to another. In a truly predictive model a functional representation of Φ that is based on the underlying physics and experimental data is required. It is needed, in particular, for applications to mine vulnerability because the loading pressure generated by a line charge is a sensitive function of bottom standoff. Because the theory is mathematically difficult and not wholly developed for these problems, we undertook an empirical study as an initial step in defining a reflection coefficient function for use in a variable Φ model.

The success shown above of the constant Φ model in representing the pressure-time and impulse-time curves in the M58 case, which was the first case studied, prompted us to apply the constant Φ model to other gage positions and to other shots. It was of interest to examine how the Φ values that were required to match the impulse measurements varied from one set of conditions to another. Calculations were performed for all pressure gage positions 2 inches from the bottom in the Eglin 1995 tests as well as for some of the gage placements that were closer to the free surface. In the 1995 Eglin tests each of the three line charge systems of interest (M58, D-Sabre, and C-Sabre) had been fired in water both 3 and 10 feet deep to provide a total of six shots. In each shot the total number of gage positions placed 2 inches above the sand was eight, and four gages were placed at shallower positions that depended upon the water depth. Table I lists the conditions of the 1995 Eglin tests that are analyzed in this report and also serves as a guide to figures showing comparisons between pressure calculations and test data.

Table I. Conditions and Figure Numbers of Analyzed 1995 Eglin Tests

System	Shot No.	Water depth (ft)	Standoff (ft)	Gage height	Figure Nos.
M58	4283	3	6	2 in	13a, A-1a
M58	4283	3	8	2 in	13b, A-1b
M58	4283	3	10	2 in	13c, A-1c
M58	4283	3	13	2 in	13d, A-1d
M58	4286	10	12	2 in	10a, A-4a
M58	4286	10	15	2 in	10b, A-4b
M58	4286	10	18	2 in	10c, A-4c
M58	4286	10	18	6 ft	10g
M58	4286	10	22	2 in	10d, A-4d
M58	4286	10	26	6 ft	10h
M58	4286	10	30	2 in	10e, A-4e
M58	4286	10	35	2 in	10f, A-4f
D-Sabre	4284	3	6	2 in	14a, A-2a
D-Sabre	4284	3	8	2 in	14b, A-2b
D-Sabre	4284	3	10	2 in	14c, A-2c
D-Sabre	4284	3	13	2 in	14d, A-2d
D-Sabre	4284	3	18	2 in	14e
D-Sabre	4284	3	23	2 in	14f, A-2e
D-Sabre	4284	10	12	2 in	11a, A-5a
D-Sabre	4284	10	15	2 in	11b, A-5b
D-Sabre	4284	10	18	2 in	11c, A-5c

Table I—Continued

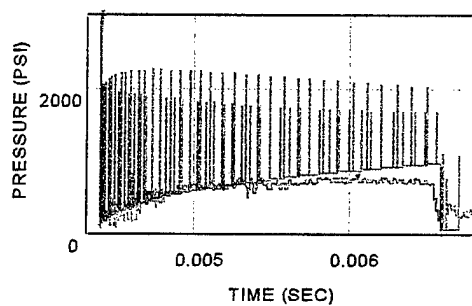
System	Shot No.	Water depth (ft)	Standoff (ft)	Gage height	Figure Nos.
D-Sabre	4284	10	22	2 in	11d, A-5d
D-Sabre	4284	10	30	2 in	11e, A-5e
D-Sabre	4284	10	35	2 in	11f, A-5f
C-Sabre	4285	3	6	2 in	15a, A-3a
C-Sabre	4285	3	8	2 in	15b, A-3b
C-Sabre	4285	3	10	2 in	15c, A-3c
C-Sabre	4285	3	13	2 in	A-3d
C-Sabre	4285	3	23	2 in	15e, A-3e
C-Sabre	4285	3	28	2 in	15f, A-3f
C-Sabre	4288	10	12	2 in	12a, A-6a
C-Sabre	4288	10	15	2 in	12b, A-6b
C-Sabre	4288	10	18	2 in	12c, A-6c
C-Sabre	4288	10	22	2 in	12d, A-6d
C-Sabre	4288	10	30	2 in	12e, A-6e
C-Sabre	4288	10	35	2 in	12f, A-6f

Comparison of Constant Φ Model Calculations with Measurements in Water 10 Feet Deep

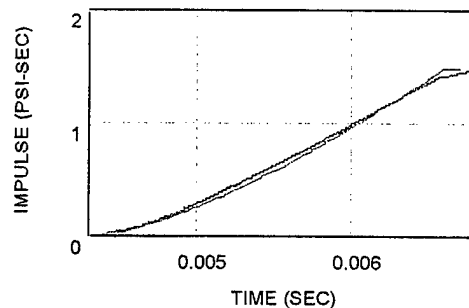
The 10-foot water depth results are shown in Figures 10 through 12. In Figure 10 calculated quantities (shown in red) are compared with measured quantities (shown in blue) for shot 4286 of the M58 system. The results that appeared above in Figures 3 and 4 are shown again in Figure 10c. Similar comparisons for shot 4287 of the discrete Sabre line charge are shown in Figure 11 and for shot 4288 of the continuous Sabre system in Figure 12.

Each figure title specifies a gage letter that identifies the gage cable and gage position. In all 10-foot water depth cases the cable A gage was at a horizontal standoff of 12 feet from the line charge axis, the B gage was at 15 feet, the C and D gages were at 18 feet, the E gage was at 22 feet, the F and G gages were at 26 feet, the H and I gages were at 30 feet, and the J gage was at 35 feet. All gages were located 2 inches from the sand bottom in the plane perpendicular to and bisecting the line charge, with the exception of the D, G, and I gages, which were in the perpendicular plane and 6 feet from the sand bottom (4 feet from the free surface). Note that the ordering of the figures below, within each shot group, is not always alphabetical. The records of shallow-depth gages and of faulty gages are usually omitted.

Figures 10a through 10f indicate that a constant value of Φ can be found that will produce good to excellent agreement between the model impulse calculations and the impulse curves derived from the experimental pressure measurements at the near-bottom gage positions of shot 4286. The model also reliably reproduces the ramp pressure history and ramp cutoff time, which coincides with the first arrival of a free surface-reflected pulse. Inability to predict the leading spike is particularly apparent in Figure 10f, where pressures are low and the leading spike causes a significant jump in the initial impulse. At such low pressures, however, gage drift may also be a contributing factor in the disagreement. As suggested earlier, it is likely that the initial spike is, in part, a consequence of the dense packing of arrivals at the leading edge of the pulse train. These, when integrated over the area of the gage crystal, may create the illusion of a broad leading spike. It may also involve the buildup of positive precursor waves, which are not included in the present model. Comparison with the measurements is, thus, complicated by these considerations and requires further study.

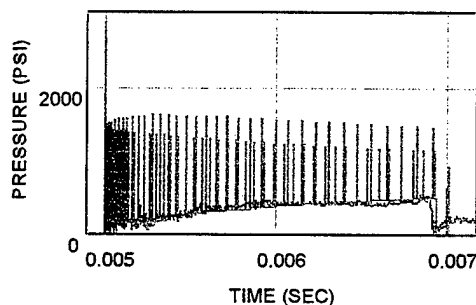


PRESSURE-TIME CURVES

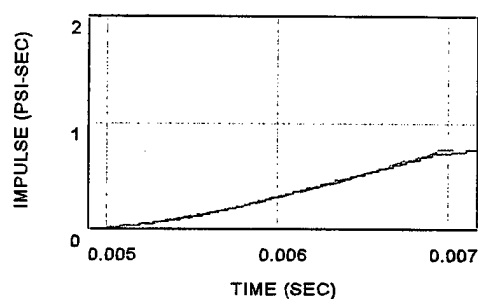


IMPULSE-TIME CURVES

a. Gage A, 12-Foot Standoff, 2-Inch Height, $\phi = -0.992$

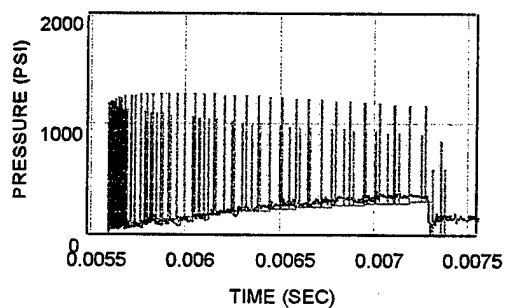


PRESSURE-TIME CURVES

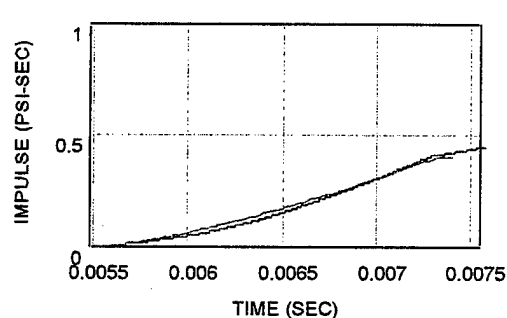


IMPULSE-TIME CURVES

b. Gage B, 15-Foot Standoff, 2-Inch Height $\phi = -0.9946$



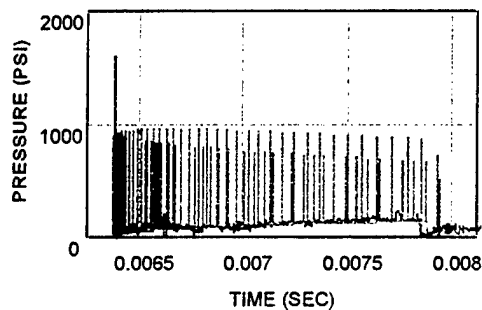
PRESSURE-TIME CURVES



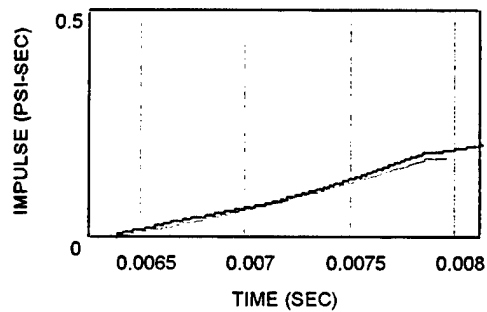
IMPULSE-TIME CURVES

c. Gage C, 18-Foot Standoff, 2-Inch Height, $\phi = -0.9963$

Figure 10. Results of M58 Shot 4286

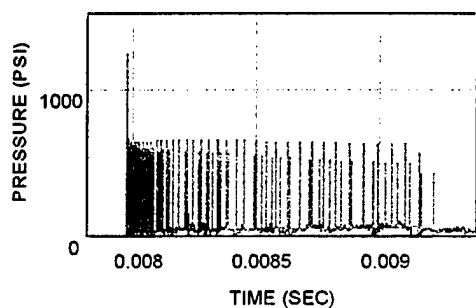


PRESSURE-TIME CURVES

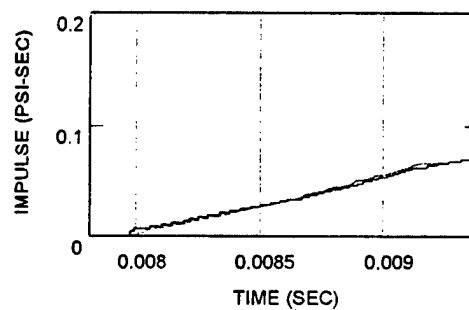


IMPULSE-TIME CURVES

d. Gage E, 22-Foot Standoff, 2-Inch Height, $\Phi = -0.998$

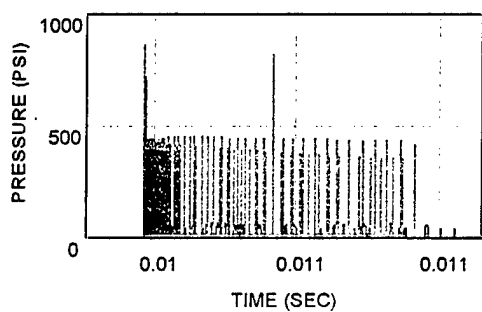


PRESSURE-TIME CURVES

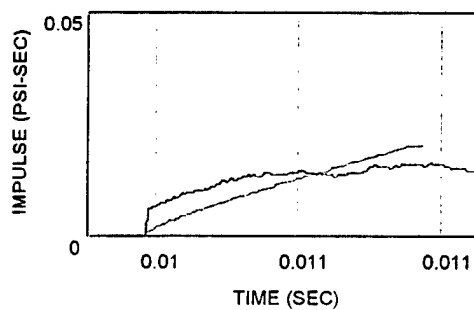


IMPULSE-TIME CURVES

e. Gage H, 30-Foot Standoff, 2-Inch Height, $\Phi = -0.999$



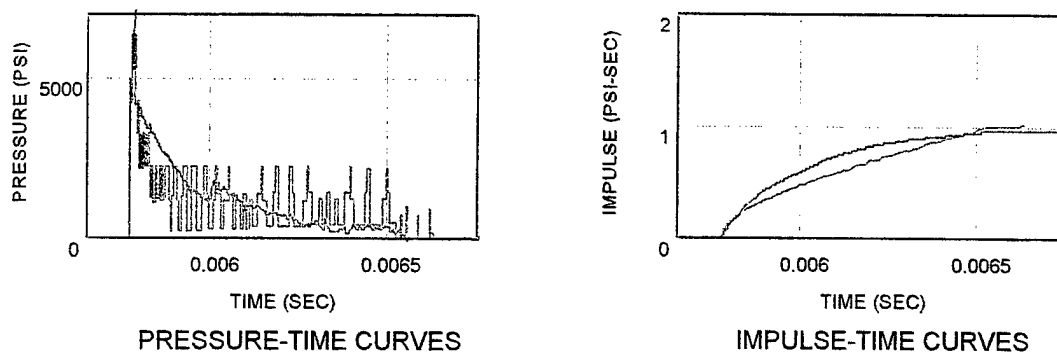
PRESSURE-TIME CURVES



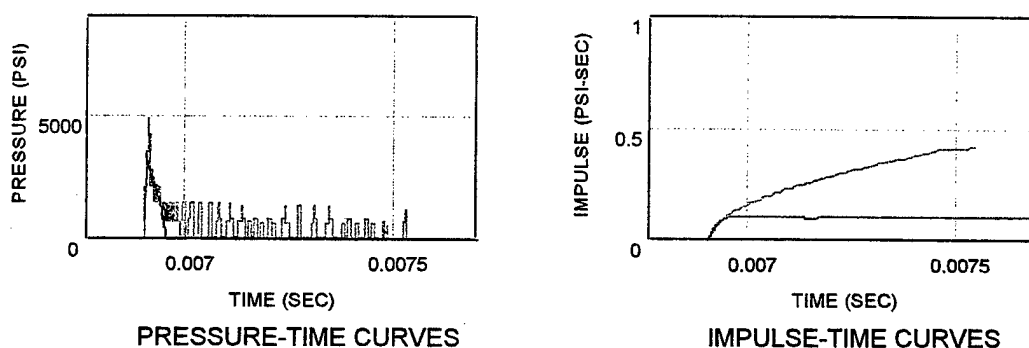
IMPULSE-TIME CURVES

f. Gage J, 35-Foot Standoff, 2-Inch Height, $\Phi = -1.0$

Figure 10. Results of M58 Shot 4286 (Continued)



g. Gage D, 18-Foot Standoff, 6-Foot Height, $\Phi = -0.995$

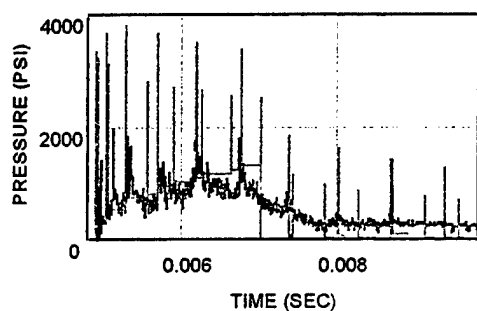


h. Gage G, 26-Foot Standoff, 6-Foot Height, $\Phi = -1.0$

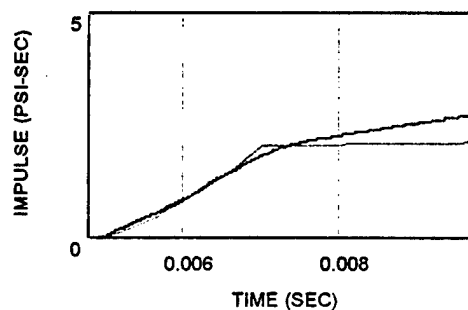
Figure 10. Results for M58 Shot 4286 (Continued)

In Figures 10g and 10h, pressure gages are located 6 feet above the bottom interface. In these cases the shapes of the wave forms differ markedly from those associated with the 2-inch gage positions. The figures show that the model is in qualitative agreement with the measurements, but the pressure wave forms and impulses in these cases do not match the measurements as well as when the gages are near the bottom. In Figure 10h an unphysical Φ value more negative than -1 would have been required to match the measured impulse-time curve. Nevertheless, the results demonstrate that the basic mechanism of pulse formation is probably being captured by the model. It is believed that the agreement could be improved with model refinement. Because our primary interest in this work has been in attacking mines at locations near the bottom, such improvements have been deferred until a later time.

Figure 11 shows comparisons between calculations and measurements for the discrete Sabre (D-Sabre) line charge system in 10 feet of water and with the gage positions 2 inches above the bottom interface. Again, calculations are shown in red and measurements in blue. It should be noted that the records in Figure 11 extend over longer time intervals than those shown in Figures 10a through 10f. The problems with late time impulse match-up evident in Figure 11 are also characteristic of the 10-foot M58 calculations, but these times are not displayed in Figures 10a through 10f.

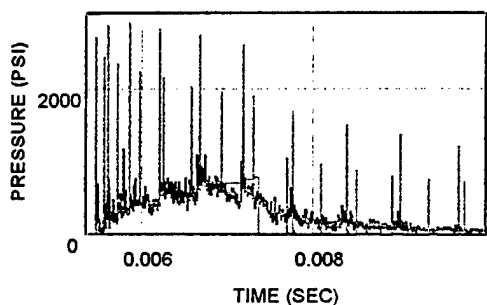


PRESSURE-TIME CURVES

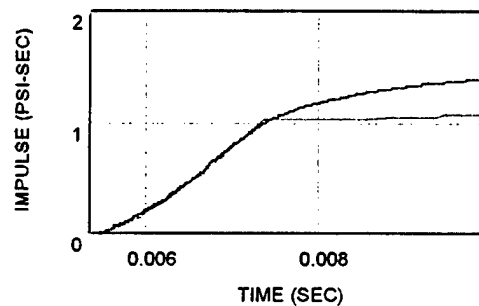


IMPULSE-TIME CURVES

a. Gage A, 12-Foot Standoff, 2-Inch Height, $\phi = -0.96$

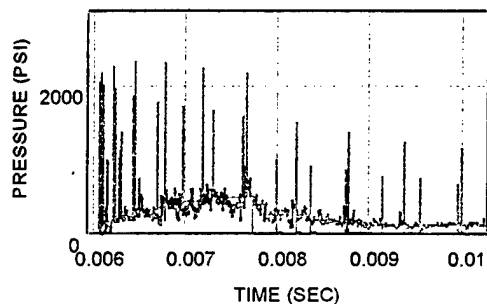


PRESSURE-TIME CURVES

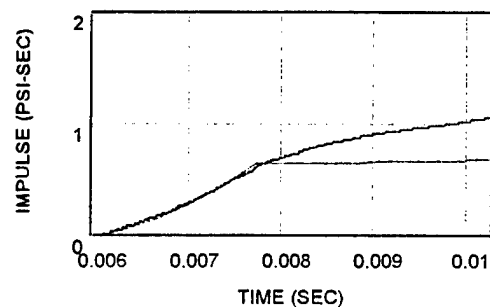


IMPULSE-TIME CURVES

b. Gage B, 15-Foot Standoff, 2-Inch Height, $\phi = -0.973$



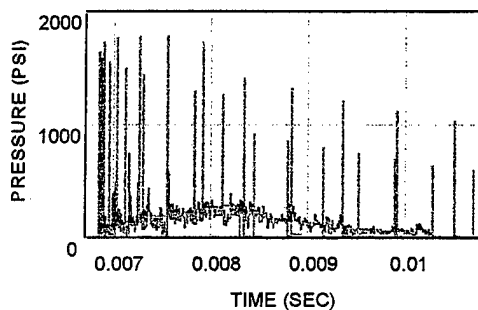
PRESSURE-TIME CURVES



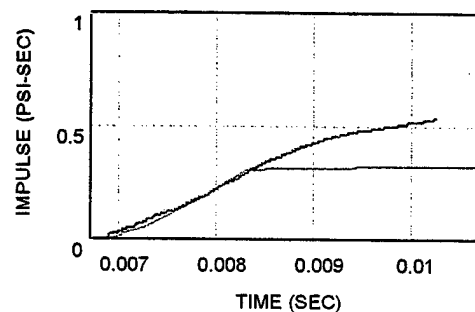
IMPULSE-TIME CURVES

c. Gage C, 18-Foot Standoff, 2-Inch Height, $\phi = -0.978$

Figure 11. Results for D-Sabre Shot 4287

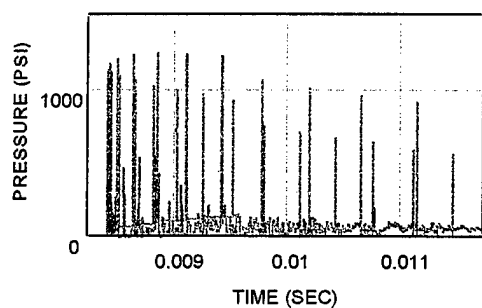


PRESSURE-TIME CURVES

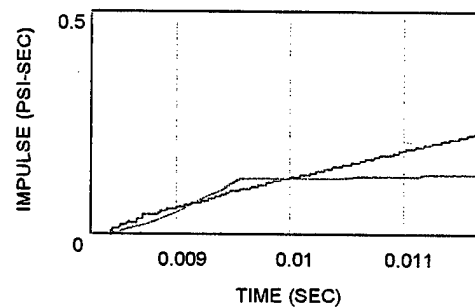


IMPULSE-TIME CURVES

d. Gage E, 22-Foot Standoff, 2-Inch Height, $\phi = -0.986$

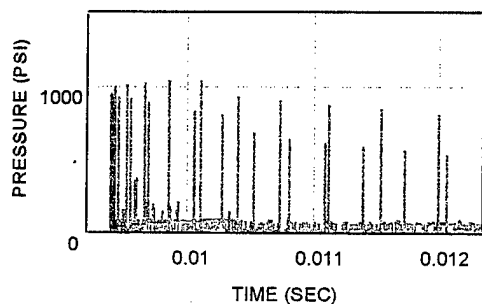


PRESSURE-TIME CURVES

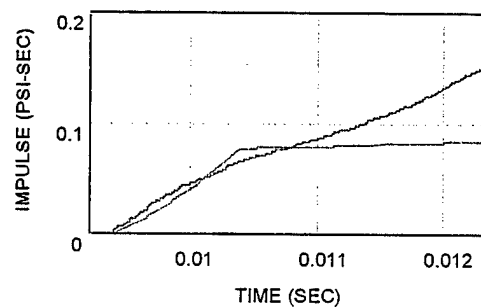


IMPULSE-TIME CURVES

e. Gage H, 30-Foot Standoff, 2-Inch Height, $\phi = -0.991$



PRESSURE-TIME CURVES



IMPULSE-TIME CURVES

f. Gage J, 35-Foot Standoff, 2-Inch Height, $\phi = -0.993$

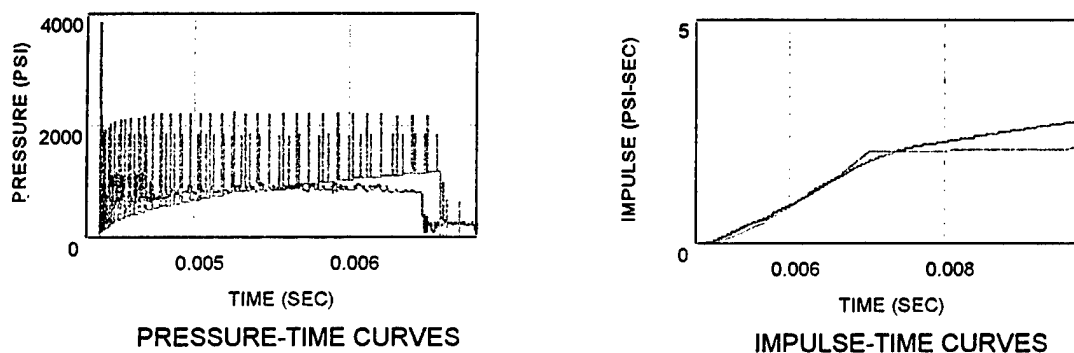
Figure 11. Results of D-Sabre Shot 4287 (Continued)

The D-Sabre system has larger charges and larger spacings between charges than the M58. Apparently because of these design differences, the D-Sabre pressure-time history differs in several respects from the M58 signature (and also from that of continuous Sabre, which is closer to the M58, as will be shown below). D-Sabre has fewer bottom-reflected arrivals between the leading edge of the pulse and surface cutoff time. In addition, the measured pressures show broadened pressure peaks, distinctly different from the calculated pressure spikes, that are possibly a result of finite amplitude effects. Because there are fewer arrivals within a unit interval of time, differences between calculated and measured arrival times are more evident for the D-Saber cases. The arrival times are quite sensitive to errors in gage positions, which may account for some of the observed differences. Another source or significant error is probably the assumption of sonic wave speeds.

The figures verify that it is possible to select constant Φ values so that the calculated impulses are in good agreement with the measured impulse time curves up to the time of surface cutoff, but thereafter the calculations fall below the measured levels which rise at a faster rate. The time of surface cutoff is not nearly as distinct in the D-Sabre measurements as it appears in the M58 records. It is felt that this may be associated with the peak broadening mechanism and, as pointed out by Britt,¹⁰ with the arrival of doubly reflected (source-to-bottom-to-surface-to-gage or source-to-surface-to-bottom-to-gage) signals after the time of surface cutoff that are not included in the present model. The absence of multiply reflected arrivals may also explain the poorer late time agreement.

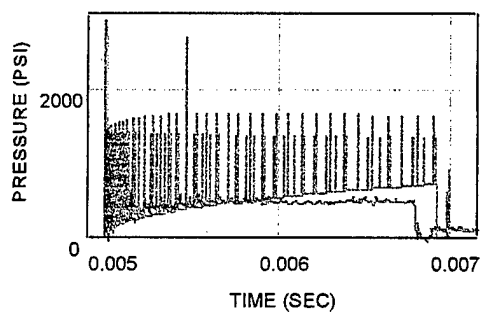
Figure 12, pertaining to the continuous Sabre system, completes the comparison of the constant Φ model calculations with the 10-foot water depth measurements. Because of the similarities of design between the C-Sabre and M58 systems, the pressure signatures shown in Figures 12 resemble those of Figures 10a through 10f. The problems with late-time match-up are again apparent.

One concludes from all 10-foot water depth comparisons (i.e., from Figures 10, 11, and 12) that the constant Φ model provides quite reasonable agreement with measured impulse-time curves for a period lasting about 2 μ s after arrival of the pulse train. It must be remembered, of course, that Φ values have been selected to promote this agreement.

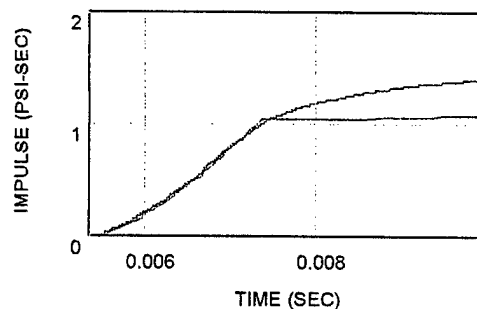


a. Gage A, 12-Foot Standoff, 2-Inch Height, $\Phi = -0.989$

Figure 12. Results for C-Sabre Shot 4288

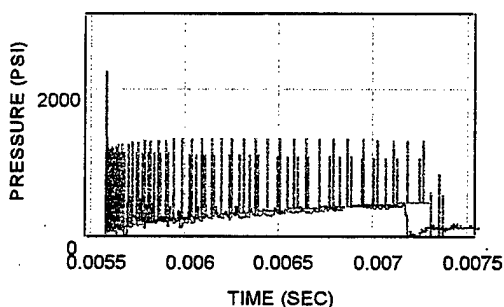


PRESSURE-TIME CURVES

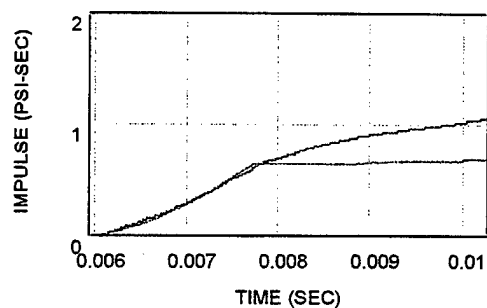


IMPULSE-TIME CURVES

b. Gage B, 15-Foot Standoff, 2-Inch Height, $\phi = -0.992$

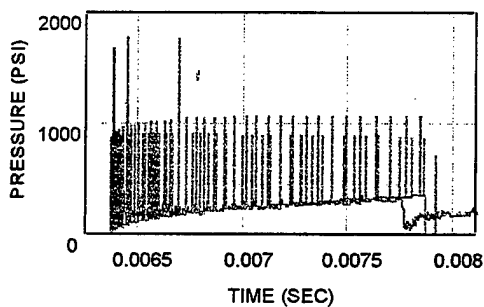


PRESSURE-TIME CURVES

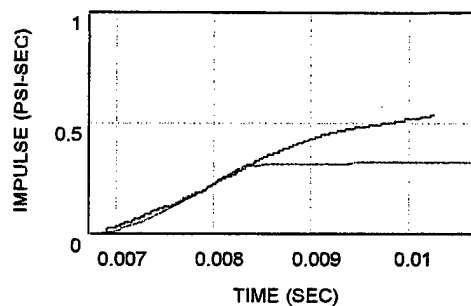


IMPULSE-TIME CURVES

c. Gage C, 18-Foot Standoff, 2-Inch Height, $\phi = -0.994$



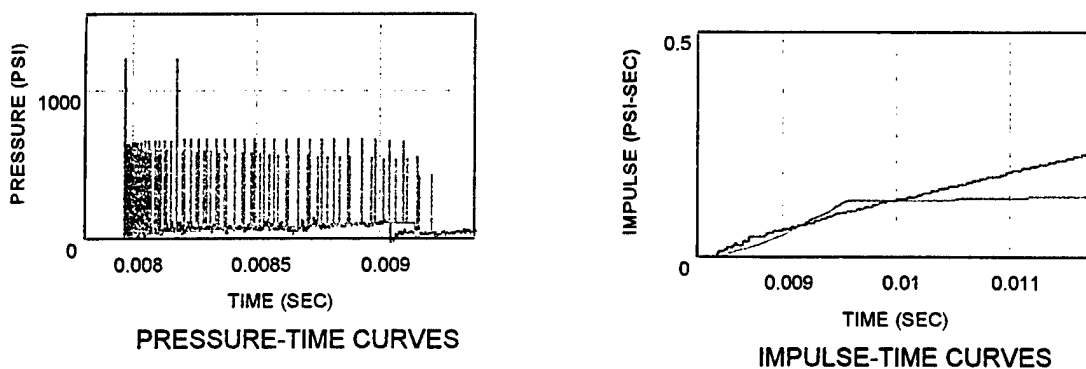
PRESSURE-TIME CURVES



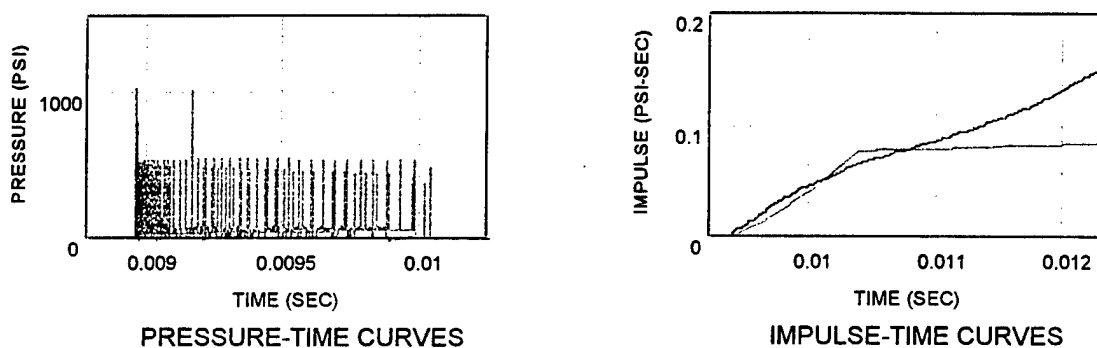
IMPULSE-TIME CURVES

d. Gage E, 22-Foot Standoff, 2-Inch Height, $\phi = -0.9945$

Figure 12. Results for C-Sabre Shot 4288 (Continued)



e. Gage H, 30-Foot Standoff, 2-Inch Height, $\Phi = -0.998$



f. Gage J, 35-Foot Standoff, 2-Inch Height, $\Phi = -0.999$

Figure 12. Results for C-Sabre Shot 4288 (Continued)

Comparison of Constant Φ Model Calculations with Measurements in Water 3 Feet Deep:

Figures 13, 14, and 15 show comparisons between calculated and measured pressures and impulses for the M58 (shot 4283), D-Sabre (shot 4284), and C-Sabre (shot 4285) line charge systems, respectively, in 3 feet of water. In these shallow water shots the gages were positioned closer to the line charge than in the 10-foot-deep cases. Gage A was at a horizontal standoff of 6 feet from the line charge axis, gage B was at 8 feet, gages C and D were at 10 feet, gage E was at 13 feet, gages F and G were at 18 feet, gages H and I were at 23 feet, and gage J was at 28 feet. With the following exceptions the gages were located 2 inches from the sand bottom in the plane perpendicular to and bisecting the line charge axis. The D, G, and I gages were located in this plane at the indicated standoffs, but at a height of 2 feet from the sand bottom (one foot from the free surface). It is seen that the F gage in the 3-foot water depth shots was at the same position as the C gage in the 10-foot water depth shots, but that all other gage positions were different.

We note that the only systematic difference between M58 shots 4283 and 4286, between D-Sabre shots 4284 and 4287, and between C-Sabre shots 4285 and 4288 is the water depth (see, e.g., Table I). This means that up until the arrivals of the first free surface reflections, these paired shots can be regarded as identical except for random differences. The pre-surface-cutoff portions of the histories shown for the 3-foot depth cases can be thought of as replicate observations (in most cases from different gage positions) of the pressure fields generated in the 10-foot water depth shots. We will use this fact in the next section to make a comment on the reproducibility of the Eglin tests. It is also useful to keep this fact in mind while examining Figure 13, where the early time M58 pressure histories are shown on expanded scales and the structures of the leading spikes are more apparent than before.

In Figure 13 (the M58 linear charge array) surface cutoff occurs approximately 0.25 to 0.45 μ s after the first arrival of the pulse train depending upon gage position. This is contrasted with approximately 1.2 to 2.2 μ s before surface cutoff for the 10-foot water depth cases. Aside from the initial spike, the buildup of the pressure ramp appears to be reasonably well approximated by the constant Φ model calculations. The calculated impulse-time curve is also in apparent agreement with the measurements over the time span shown in the figures. In fact, however, the impulse falls below the measurements at later times for the M58 cases and also, as will be seen, for the shallow continuous Sabre cases.

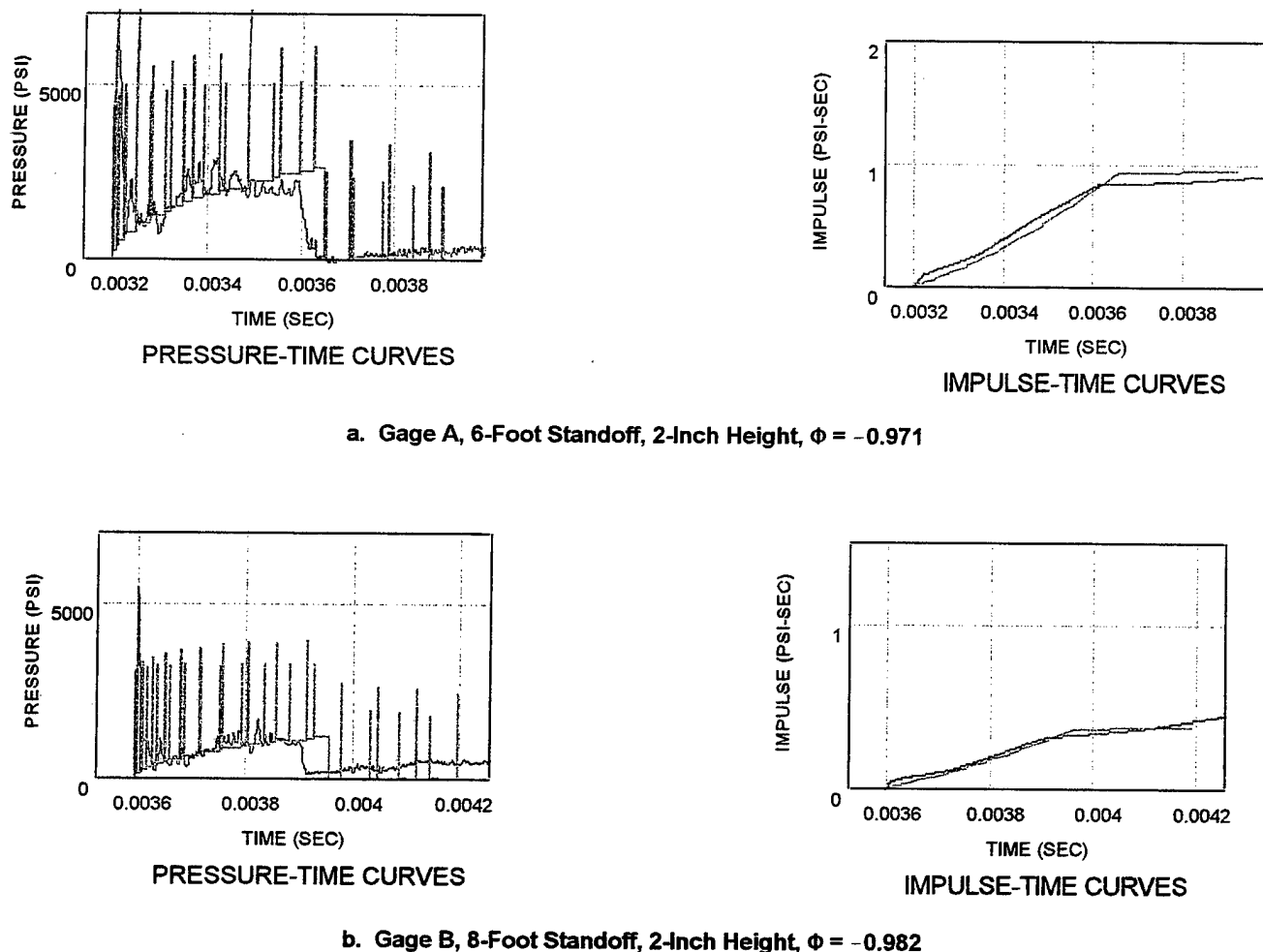
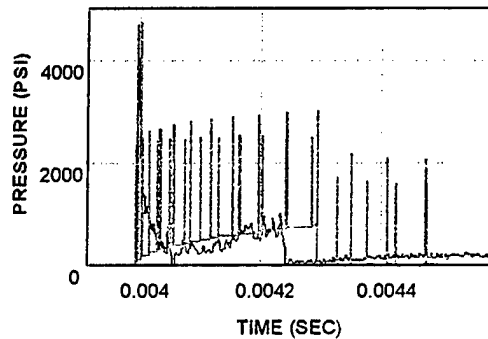
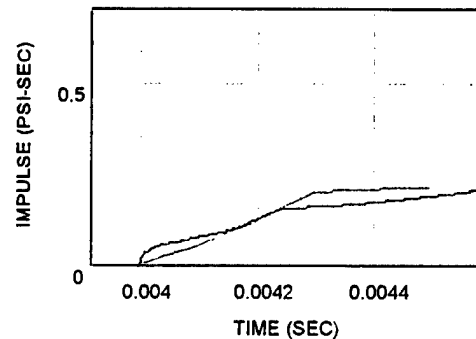


Figure 13. Results for M58 Shot 4283

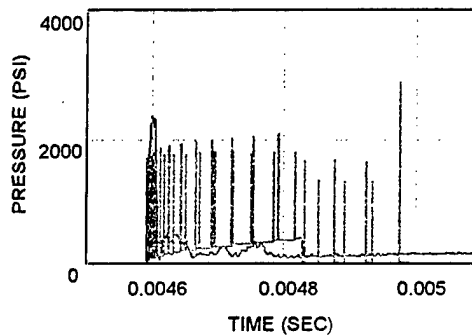


PRESSURE-TIME CURVES

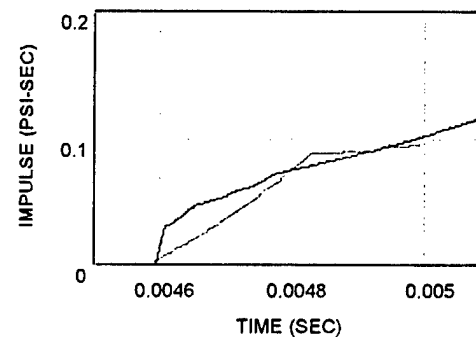


IMPULSE-TIME CURVES

c. Gage C, 10-Foot Standoff, 2-Inch Height, $\phi = -0.985$



PRESSURE-TIME CURVES

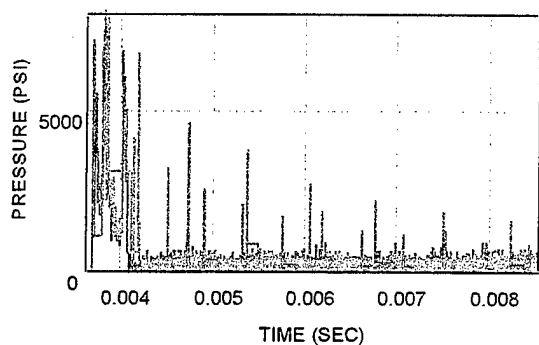


IMPULSE-TIME CURVES

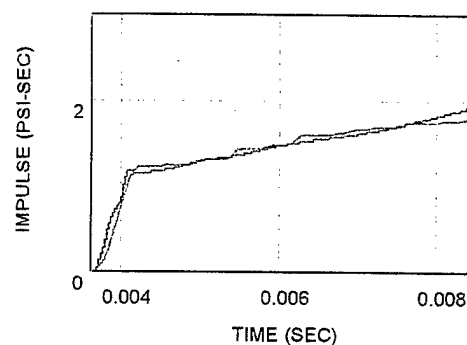
d. Gage E, 13-Foot Standoff, 2-Inch Height, $\phi = -0.99$

Figure 13. Results for M58 Shot 4283 (Continued)

Figures 14 (the D-Sabre linear array) and 15 (the C-Sabre linear array) demonstrate the behavior of the model out to later times. At present this behavior is not fully understood. The D-Sabre impulse calculations are in excellent agreement with the experimental measurements, although the agreements between the pressure-time curves, from which the impulse-time curves were integrated, are less convincing. Conversely, the C-Sabre (and, although not shown, the M58) calculated impulses lie considerably below the measurements at later times, while the pressure-time curves at early times are in quite reasonable agreement. To obtain these results, calculations were stopped after the arrival of the 20th free-surface-reflected wave in Figure 14 (and also Figure 13) and after the arrival of the 120th free-surface-reflected wave in Figure 15. Six times the number of free-surface-reflected arrivals were necessary in the (Figure 15) C-Sabre calculations to create record lengths comparable to the D-Sabre calculations because the C-Sabre array contains six times the number of charges as contained in the D-Sabre array. The agreement between the C-Sabre calculated and measured impulses seems to improve as the standoff from the line charge axis is increased. While the underprediction of late time impulse by the M58 and C-Sabre models might be explained by the absence of multiple reflection arrivals as suggested by Britt,¹⁰ it is not understood why the D-Sabre model performs so well without the multiple reflections included.

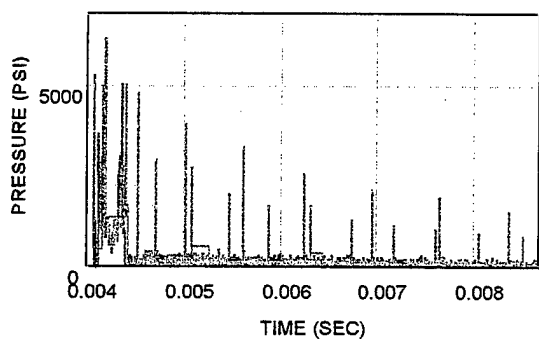


PRESSURE-TIME CURVES

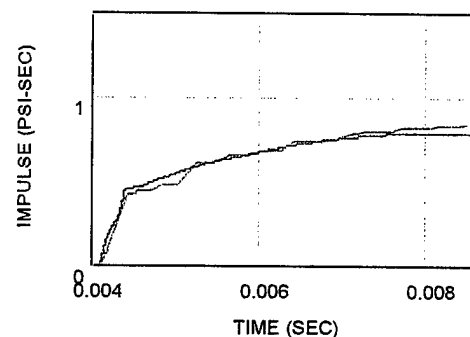


IMPULSE-TIME CURVES

a. Gage A, 6-Foot Standoff, 2-Inch Height, $\phi = -0.85$

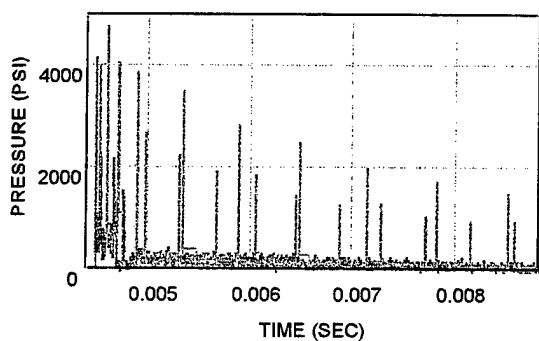


PRESSURE-TIME CURVES

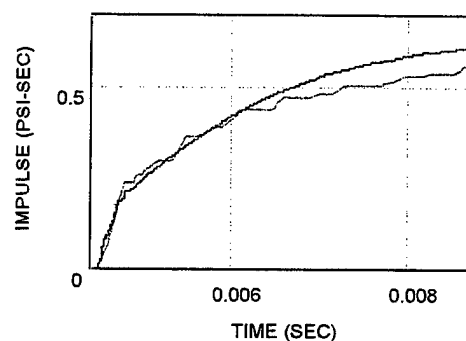


IMPULSE-TIME CURVES

b. Gage B, 8-Foot Standoff, 2-Inch Height, $\phi = -0.912$



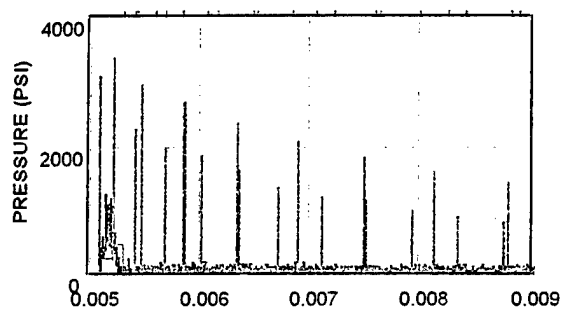
PRESSURE-TIME CURVES



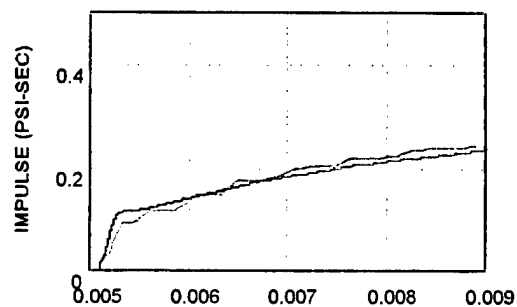
IMPULSE-TIME CURVES

c. Gage C, 10-Foot Standoff, 2-Inch Height, $\phi = -0.93$

Figure 14. Results of D-Sabre Shot 4284

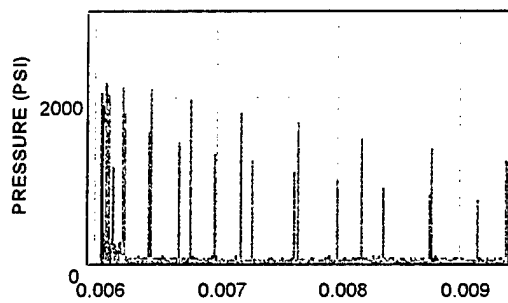


PRESSURE-TIME CURVES

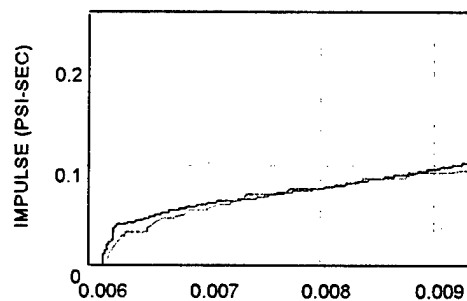


IMPULSE-TIME CURVES

d. Gage E, 13-Foot Standoff, 2-Inch Height, $\phi = -0.96$

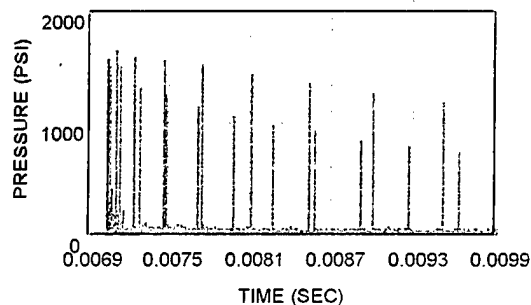


PRESSURE-TIME CURVES

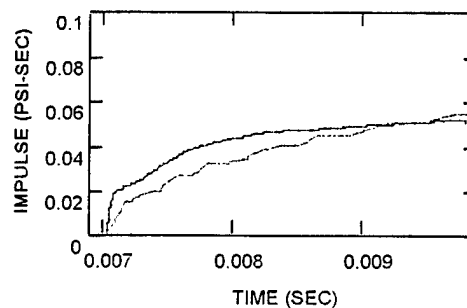


IMPULSE-TIME CURVES

e. Gage F, 18-Foot Standoff, 2-Inch Height, $\phi = -0.978$



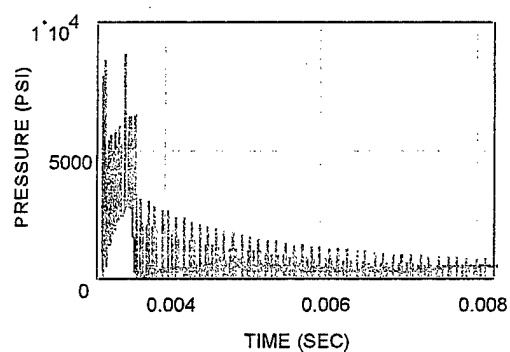
PRESSURE-TIME CURVES



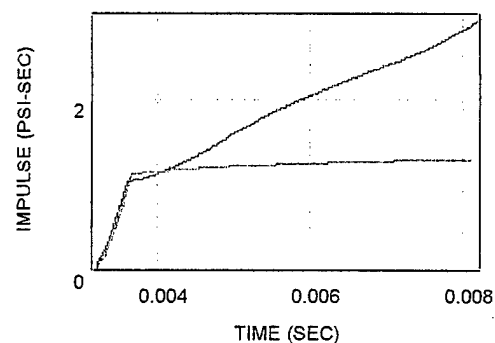
IMPULSE-TIME CURVES

f. Gage H, 23-Foot Standoff, 2-Inch Height, $\phi = -0.985$

Figure 14. Results of D-Sabre Shot 4284 (Continued)

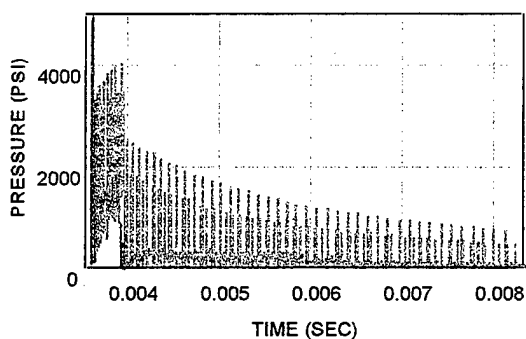


PRESSURE-TIME CURVES

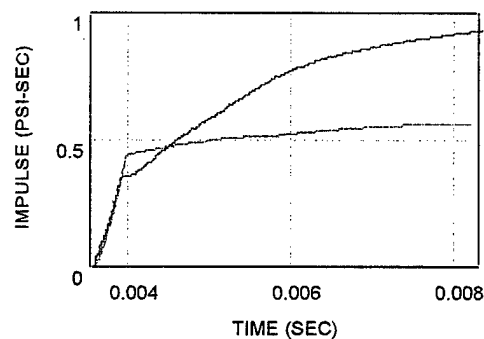


IMPULSE-TIME CURVES

a. Gage A, 6-Foot Standoff, 2-Inch Height, $\phi = -0.96$

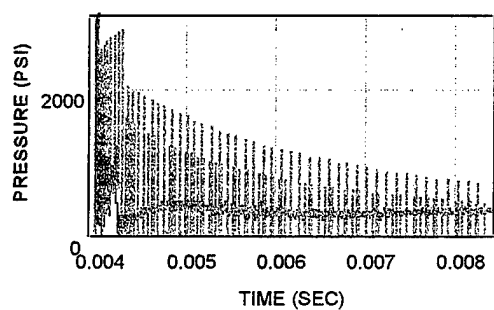


PRESSURE-TIME CURVES

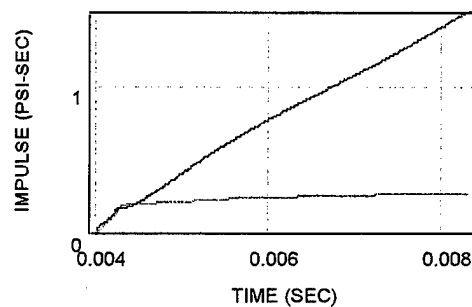


IMPULSE-TIME CURVES

b. Gage B, 8-Foot Standoff, 2-Inch Height, $\phi = -0.975$



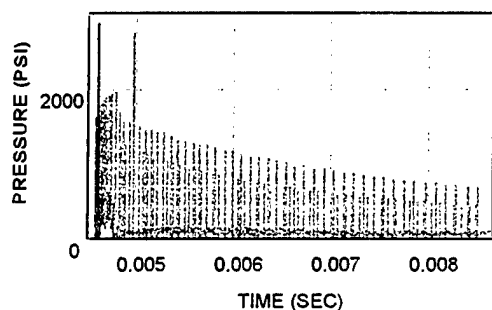
PRESSURE-TIME CURVES



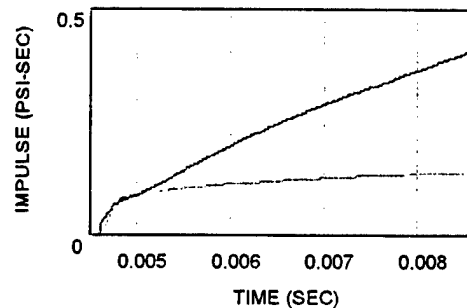
IMPULSE-TIME CURVES

c. Gage C, 10-Foot Standoff, 2-Inch Height, $\phi = -0.985$

Figure 15. Results for C-Sabre Shot 4285

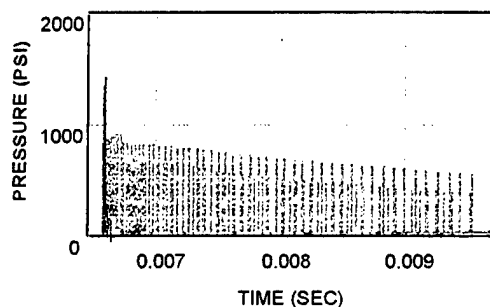


PRESSURE-TIME CURVES

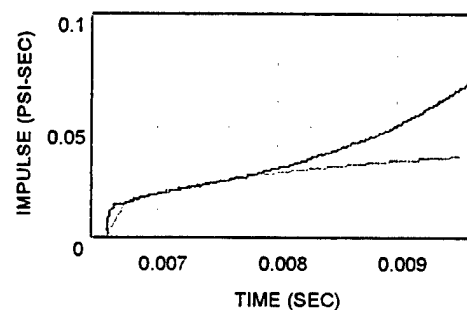


IMPULSE-TIME CURVES

d. Gage E, 13-Foot Standoff, 2-Inch Height, $\phi = -0.99$

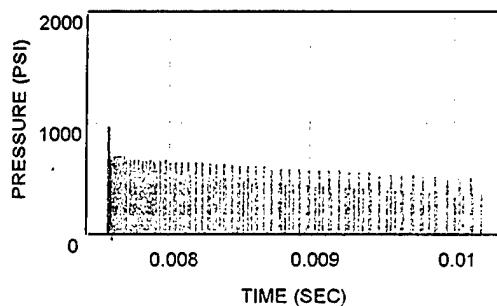


PRESSURE-TIME CURVES

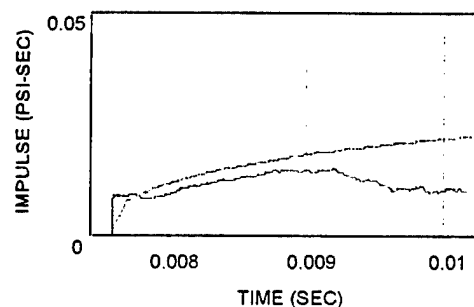


IMPULSE-TIME CURVES

e. Gage H, 23-Foot Standoff, 2-Inch Height, $\phi = -0.9965$



PRESSURE-TIME CURVES



IMPULSE-TIME CURVES

f. Gage J, 28-Foot Standoff, 2-Inch Height, $\phi = -0.999$

Figure 15. Results for C-Sabre Shot 4285 (Continued)

MODEL CONSISTENCY AND MEASUREMENT REPRODUCIBILITY

It was noted earlier that pressure time curves for 3- and 10-foot water depth cases of the same linear charge array system should be identical for gages at the same positions before the arrival of surface-reflected waves. This fact provides a means of judging the reproducibility and consistency of the measurements made in the 1995 Eglin test series and, unexpectedly, also of the modeling analysis. Figure 16 shows the records and calculations associated with the F gage in D-Sabre shot 4284 and the C gage in D-Sabre shot 4287. Shot 4284 was at a water depth of 3 feet and shot 4287 was at 10 feet. Both gages were at a standoff of 18 feet and were 2 inches above the sand. Unfortunately, because of the presence of high frequency electrical interference in the F gage records of the other shallow shots, these are the only two records that can be so compared. No other gages were placed at identical positions.

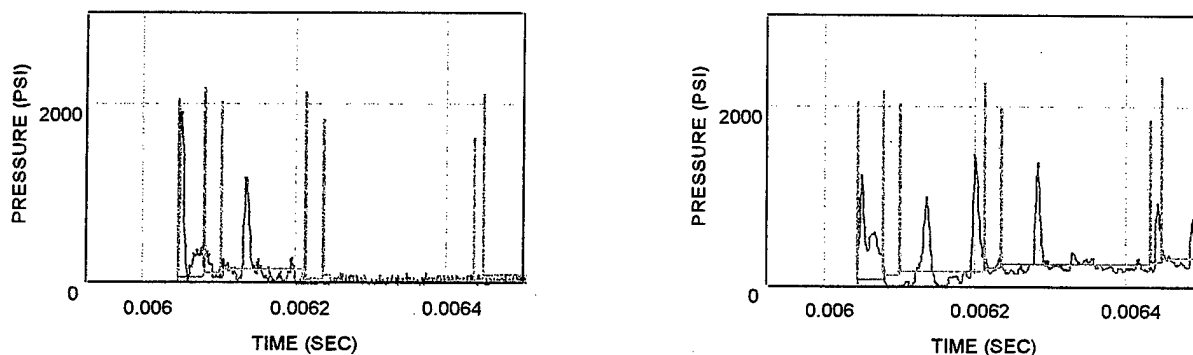


Figure 16. Comparison of Identical Gage Position Results for D-Sabre Shots 4284 (Left) and 4287 (Right)

Figure 16 reveals quite close agreement between the two experimentally measured pressure histories at early times (shown in blue). The second peaks are particularly comparable. The disagreement between leading peak pressures (and also of the second peak pressures) may be a result of the 1- μ s gage sampling rate used, reflected in the visible stepwise fine structures, which appears to be marginally adequate to effect resolution of the peaks. The absence of the third peak in the left figure can be attributed to surface cutoff, which always occurred in advance of the calculated cutoff time due to the supersonic speeds of the actual waves. Based on the agreement of the pressures of the second peaks, one might tentatively conclude that pressures from linear charge arrays at Eglin would be reproducible from shot to shot. The two D-Sabre shots were conducted one week apart and in separately prepared sites of the Eglin test area.

The consistency of the modeling analyses applied to both cases is seen in Figures 11c and 14e, where it is found that the reflection factors selected by matching impulse time curves were both $\Phi = -0.978$, i.e., identical to the third decimal place. These assignments were carried out independently and before it was realized that the comparisons in Figure 16 could be made. The fact that the impulse-time curve in Figure 11c is quite dissimilar in shape from that in Figure 14e due to the difference in surface cutoff times lends confidence to the modeling approach.

Because the same Φ values were used, the calculated pressures in both shots were identical at early times. Following surface cutoff, the pressure ramp in the left graph of Figure 16 is eliminated by the arrival of surface-reflected tension waves. The pressure spikes associated with the direct and bottom-reflected arrivals, however, remain.

DEVELOPMENT OF THE VARIABLE Φ MODEL

The strategy followed for development of a variable Φ model was to associate each constant Φ model reflection coefficient value appearing in Figures 10 through 15 with an appropriate reflection angle γ and determine functional forms consistent with all such fitted points that could be used in the variable Φ model code. In the code different reflection coefficient values would then be assigned to the bottom-reflected ray of each charge of the system by inserting the reflection angle of the ray into the functional form. The complication in this approach is that each impulse time curve and fitted Φ value is, in fact, associated with a range of reflection angles. Nevertheless, this information was useful in choosing final functional forms that seemed to produce suitable overall matches with the data. While a more formal statistical procedure for estimating the functional forms could certainly have been pursued, the approach taken seemed more direct and less demanding from a programming standpoint with the Mathcad (Version 6+) software being used.

An examination of the reflection coefficient values (Φ) and reflection angle (γ) ranges for all six shots suggested that each line charge system required a separate functional relationship between Φ and γ to produce the best agreement with the data. The underlying reason for this is not completely clear. But because the levels of sand compaction caused by the explosions (which could affect the values of Φ) would be different for each charge system due to differences in explosive type, charge weight, and system configuration, the use of separate functional forms appears reasonable.

The fitted reflection coefficients and reflection angle ranges associated with the M58, D-Sabre, and C-Sabre systems are shown in Figures 17, 18, and 19 respectively. In each of these the γ ranges appear as horizontal lines bounded by o symbols if the measurement was associated with a 10-foot water depth case and x symbols if it was associated with a 3-foot water depth case. In the latter the horizontal lines are also heavier in weight so that they can be easily distinguished when overlapping with the 10-foot case lines occurs. The end points of each range represent the maximum and minimum values of γ for bottom-reflected waves that arrive between the leading edge of the pulse train and the time of surface cutoff. This measure of range was chosen because it reflected the portion of the pressure history best fitted by the model.

The black curves appearing in Figures 17, 18, and 19 are quadratic forms, suggested by the data, that were observed to provide the best overall fits to the impulse time data using the variable Φ model. The specific equations used in each case are indicated below:

$$\Phi_{M58} = 14\gamma^2 + 0\gamma - 1 \quad (16)$$

$$\Phi_{D-Sabre} = 22\gamma^2 + 0.2\gamma - 1 \quad (17)$$

$$\Phi_{C-Sabre} = 15\gamma^2 + 0.1\gamma - 1 \quad (18)$$

Appendix A contains the results of calculations made with the variable Φ model in which the reflection coefficients were determined for each individual charge and gage position using Equations 16, 17, and 18. Comparison of Appendix A with Figures 10 through 15 shows that the variable Φ model slightly underperforms the constant Φ model in terms of overall agreement with the measured impulses. But in most cases the performances are comparable.

Figures 17, 18, and 19 indicate that the best agreement of the variable Φ model pressures with the measured data was obtained by associating the fitted Φ values (determined with the constant Φ model) with the highest values of reflection angles. That is, the best fit functional forms are located along the right edges of the plotted ranges of γ in all three figures. The initial expectation was that the best fit curves would pass through midrange values that were representative, in some average sense, of the overall fit. It is suggested that the largest values of γ provide the best fits because they are the values associated with the earliest and most rapid rise of the pressure ramp and to which the overall shape of the ramp is most sensitive.

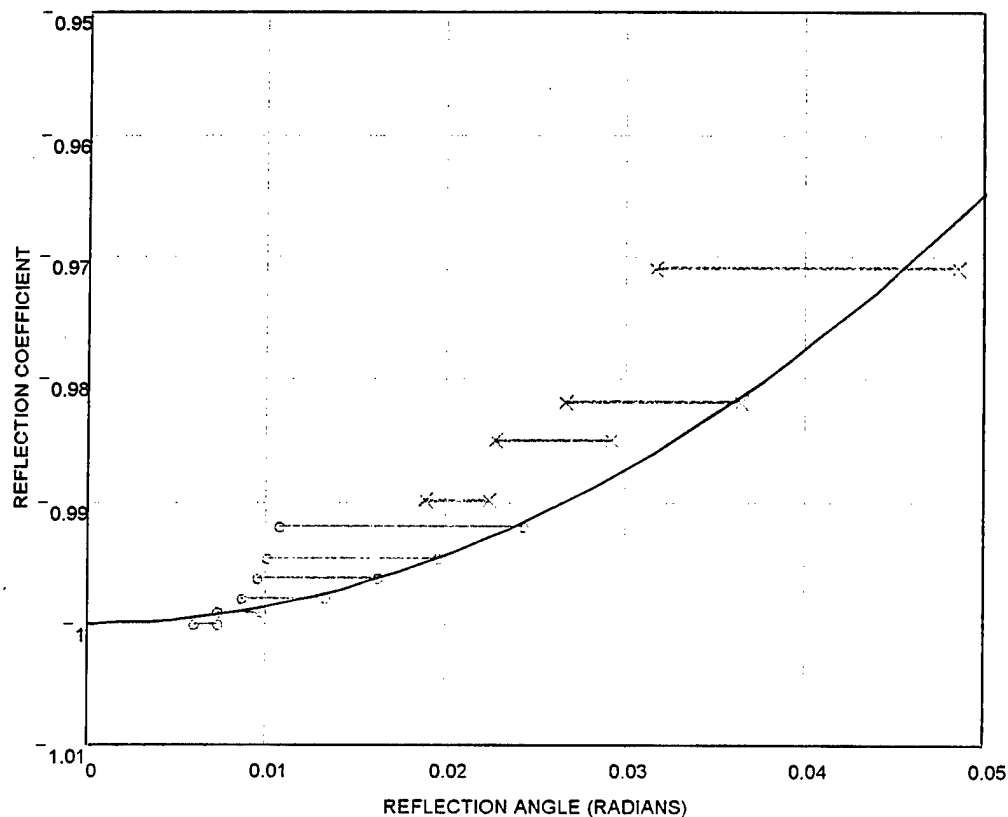


Figure 17. M58 Reflection Coefficients Versus Angle

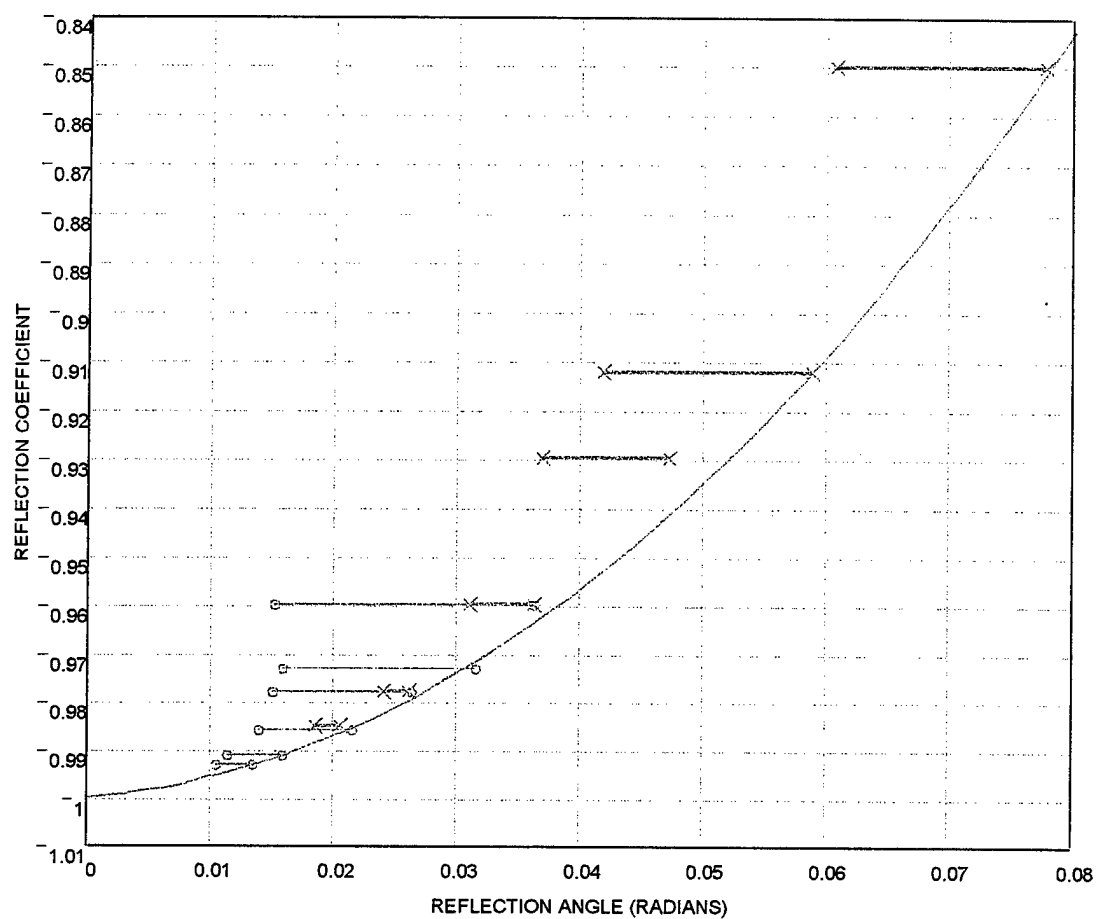


Figure 18. D-Sabre Reflection Coefficients Versus Angle

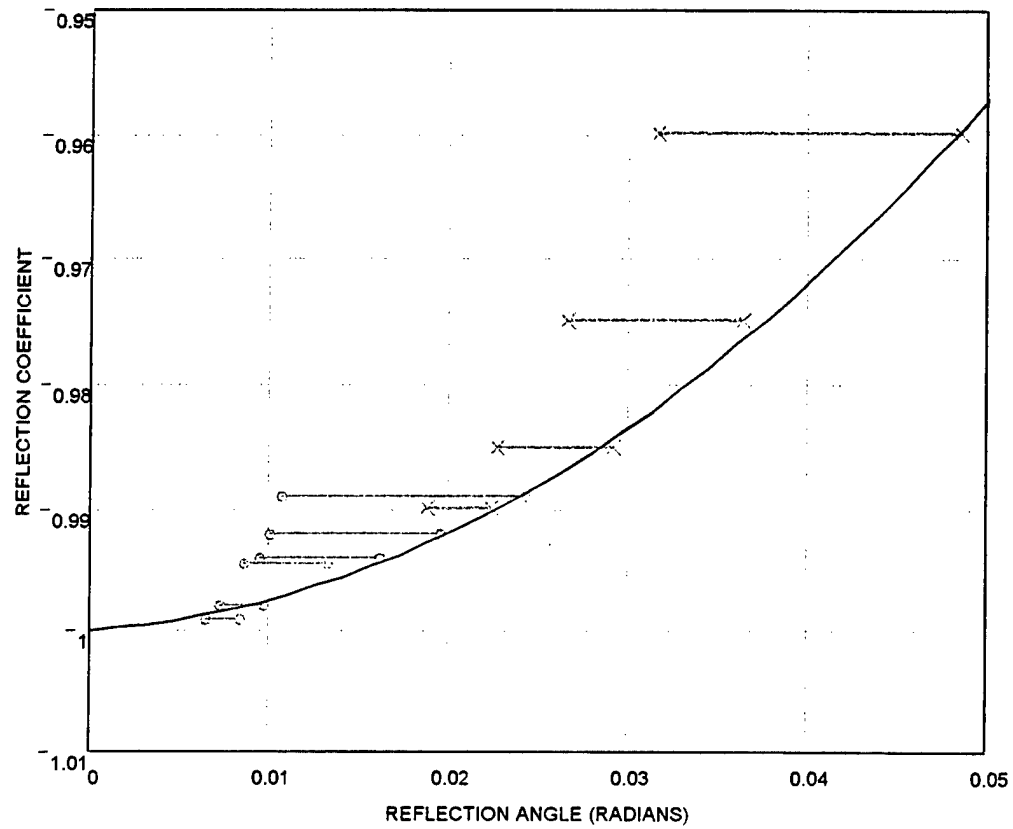


Figure 19. C-Sabre Reflection Coefficients Versus Angle

CONCLUSIONS

It was found that ray tracing modeling techniques could be effectively used to represent the pressure histories generated by linear arrays of explosive charges. It is concluded that—

- Ray tracing techniques can be used to provide rapid computations of explosive array pressure histories with accuracies that are sufficient for the analysis of mine structural responses.
- It is expected that the method would also be effective for representing the pressures associated with other charge configurations and geometries such as DET arrays, nonlinear arrays, and arrays on sloped bottoms.
- The theory of this modeling approach should be pursued to permit the reflection coefficient to be expressed as a function of water and sand mechanical properties.

REFERENCES

1. Personal communication with Joel Gaspin, Code 420, IHDNSWC.
2. Arons, A.B., and Yennie, D.R., "Phase Distortion of Acoustic Pulses Obliquely Reflected from a Medium of Higher Sound Velocity," *Journal of the Acoustical Society of America*, Vol. 22, 1950.
3. Rosenbaum, J.H., *Shockwave Propagation in Shallow Water I*, NAVORD Report 4353, August 1956.
4. Cagniard, L., Flinn, E.A., and Dix, C.H., *Reflection and Refraction of Progressive Seismic Waves*, McGraw Hill Book Company, Inc., New York, 1962.
5. Snay, H.G., and Kriebel, A.R., *Surface Reflection of Underwater Shock Waves (U)*, NOLTR 70-31, March 1970.
6. Britt, J.R., and Snay, H.G., *Bottom Reflection of Underwater Explosion Shock Waves, Computer Program*, NOLTR 71-110, July 1971.
7. Britt, J.R., *Linear Theory of Bottom Reflections*, NOLTR 69-44, May 1989.
8. Britt, J.R., Eubanks, R.J., and Lumsden, M.G., *Underwater Shock Wave Reflection and Refraction in Deep and Shallow Water, Volume I - A User's Manual for the REFMS Code (Version 4.0)*, Defense Nuclear Agency Report DNA-TR-91-15-V1, June 1991.
9. Cole, R.H., *Underwater Explosions*, Dover Publications, New York, 1949.
10. Personal communication with J.R. Britt, SAIC, July 1997.

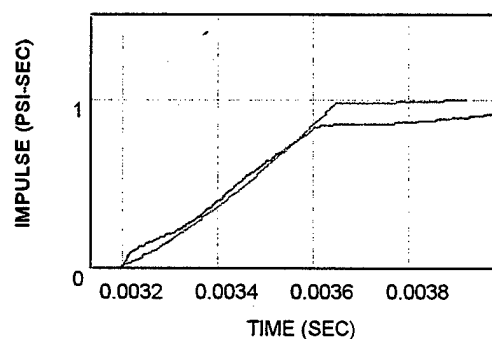
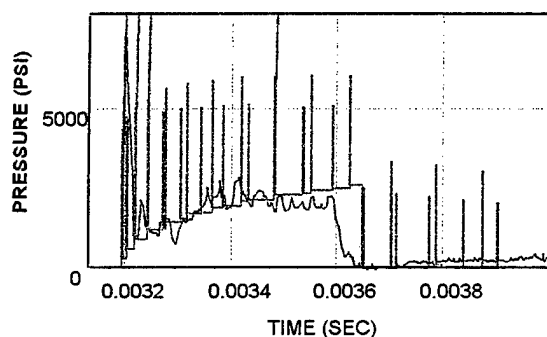
Appendix A

COMPARISON OF VARIABLE Φ MODEL CALCULATIONS WITH MEASUREMENTS

This page intentionally left blank.

COMPARISON OF VARIABLE Φ MODEL CALCULATIONS WITH MEASUREMENTS

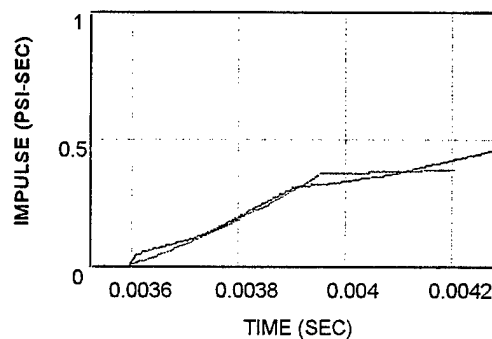
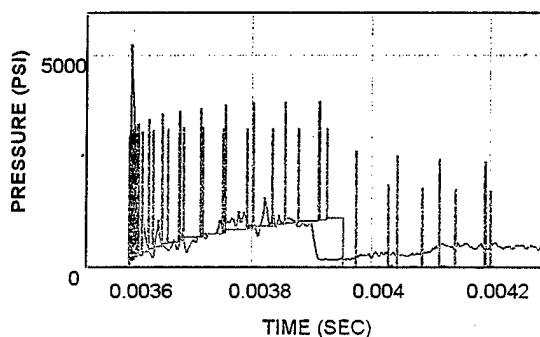
Figures A-1 through A-6 show comparisons of calculations made using the variable Φ model with measurements for the conditions of the 1995 Eglin mine vulnerability tests.¹ The numeral of each figure designation pertains to the shot order followed in the Eglin tests. As an example, Figures A-1a through A-1f show measurements recorded during the first shot of the test series. The ending letter in the designation denotes the cable and gage as explained in the text. Blue curves are the measurements and red traces are the calculations. The figure titles indicate the line charge array system, the shot number, and the gage position.



PRESSURE-TIME CURVES

IMPULSE-TIME CURVES

a. Gage A, 6-Foot Standoff, 2-Inch Height

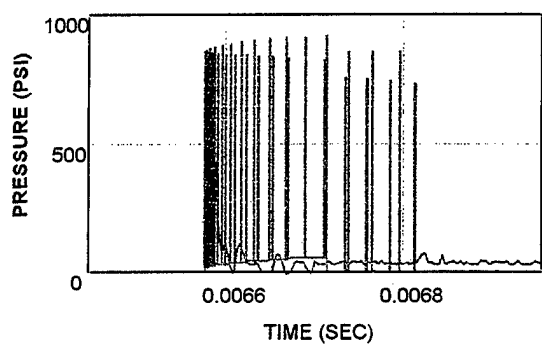


PRESSURE-TIME CURVES

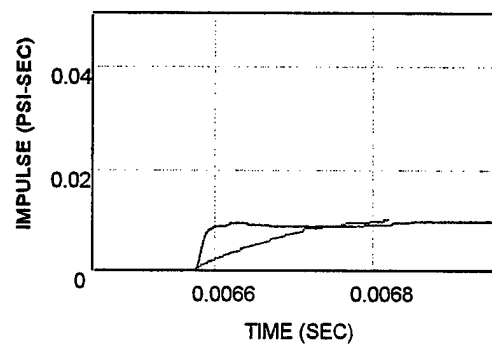
IMPULSE-TIME CURVES

b. Gage B, 8-Foot Standoff, 2-Inch Height

Figure A-1. Results for M58 Shot 4283 with Variable ϕ

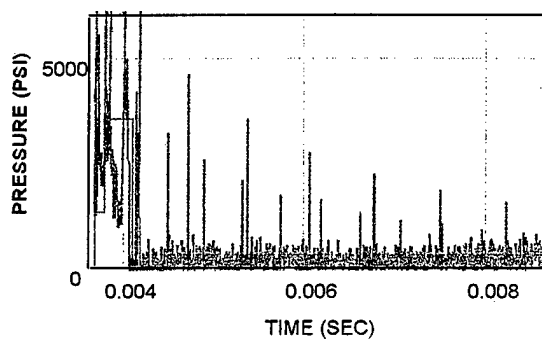


PRESSURE-TIME CURVES

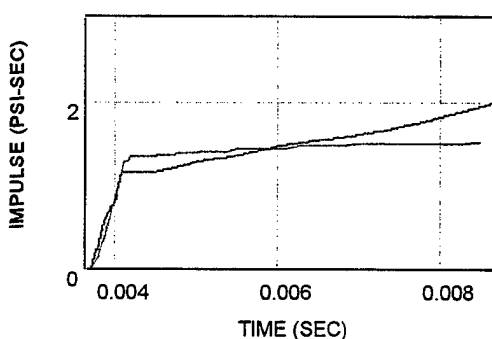


IMPULSE-TIME CURVES

f. Gage J, 28-Foot Standoff, 2-Inch Height

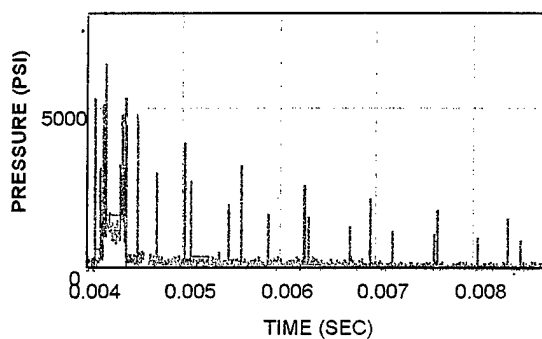
Figure A-1. Results for M58 Shot 4283 with Variable ϕ (Continued)

PRESSURE-TIME CURVES

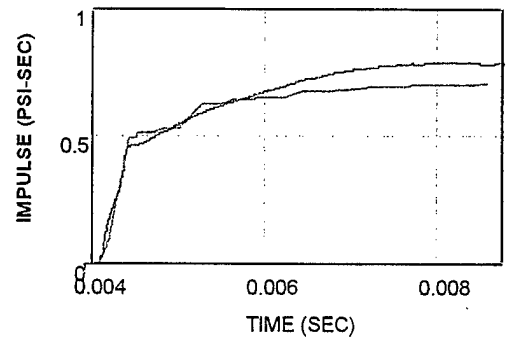


IMPULSE-TIME CURVES

a. Gage A, 6-Foot Standoff, 2-Inch Height



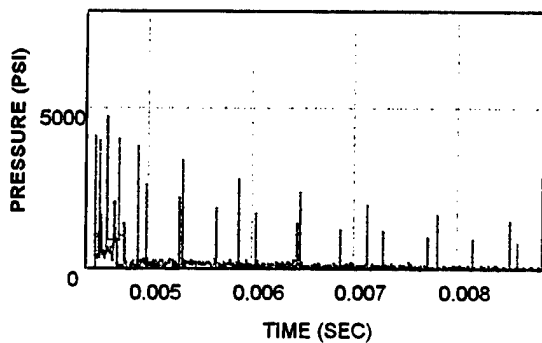
PRESSURE-TIME CURVES



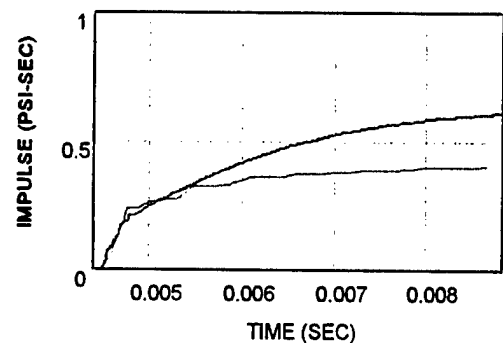
IMPULSE-TIME CURVES

b. Gage B, 8-Foot Standoff, 2-Inch Height

Figure A-2. Results for D-Sabre Shot 4284 with Variable ϕ

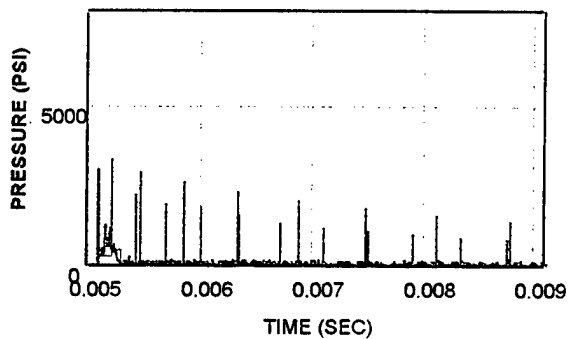


PRESSURE-TIME CURVES

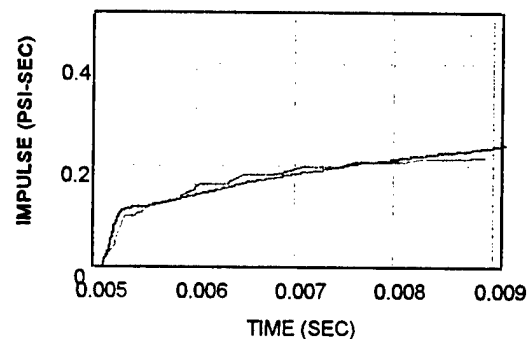


IMPULSE-TIME CURVES

c. Gage C, 10-Foot Standoff, 2-Inch Height

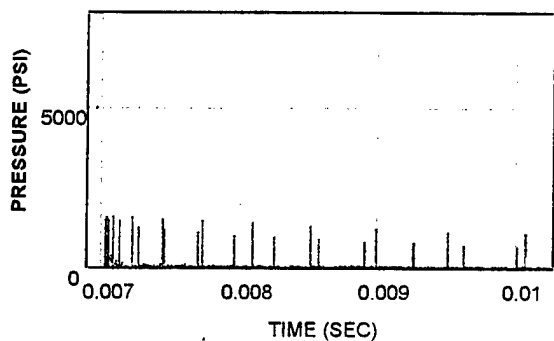


PRESSURE-TIME CURVES

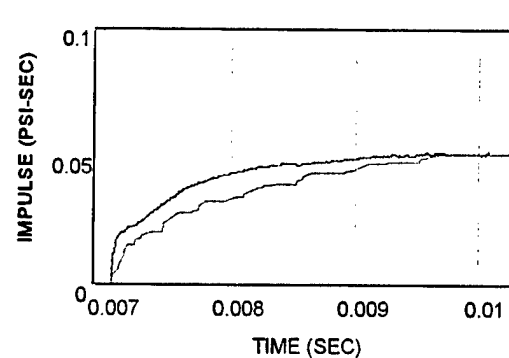


IMPULSE-TIME CURVES

d. Gage E, 13-Foot Standoff, 2-Inch Height



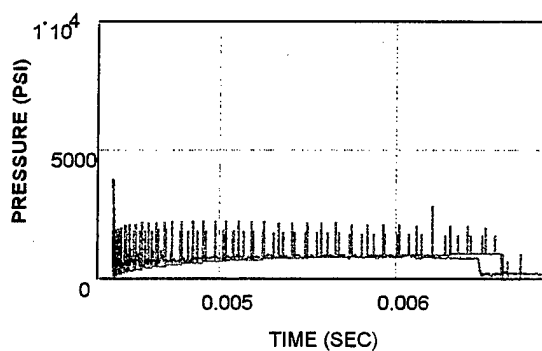
PRESSURE-TIME CURVES



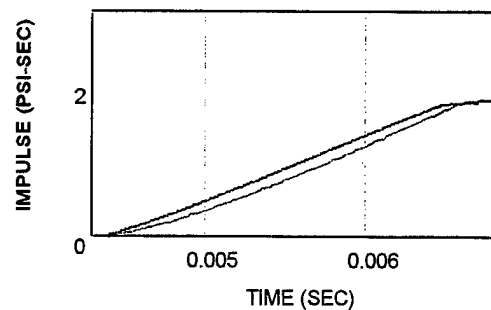
IMPULSE-TIME CURVES

e. Gage H, 23-Foot Standoff, 2-Inch Height

Figure A-2. Results for D-Sabre Shot 4284 with Variable ϕ (Continued)

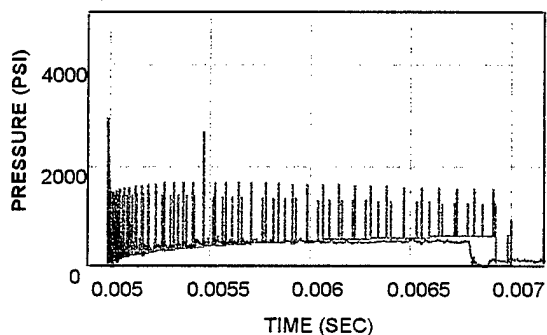


PRESSURE-TIME CURVES

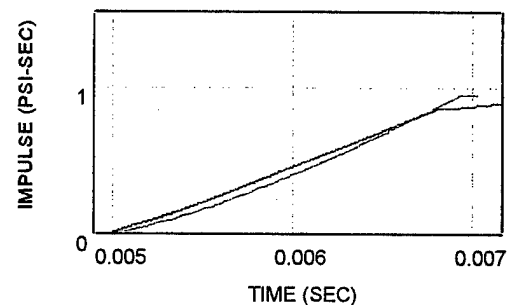


IMPULSE-TIME CURVES

a. Gage A, 6-Foot Standoff, 2-Inch Height

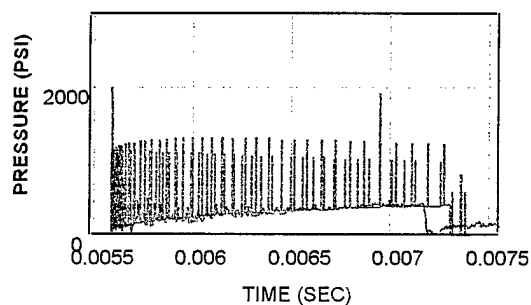


PRESSURE-TIME CURVES

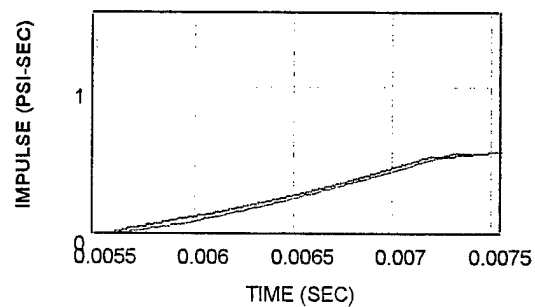


IMPULSE-TIME CURVES

b. Gage B, 8-Foot Standoff, 2-Inch Height



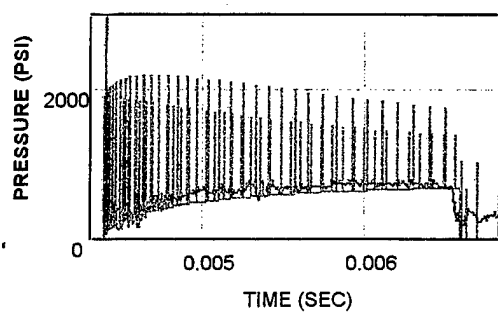
PRESSURE-TIME CURVES



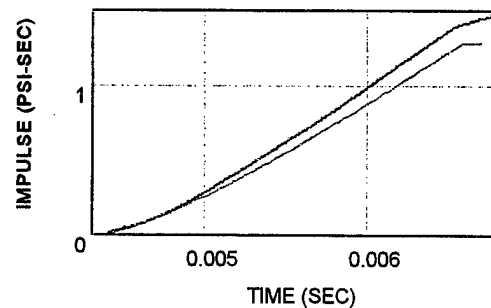
IMPULSE-TIME CURVES

c. Gage C, 10-Foot Standoff, 2-Inch Height

Figure A-3. Results for C-Sabre Shot 4285 with Variable ϕ

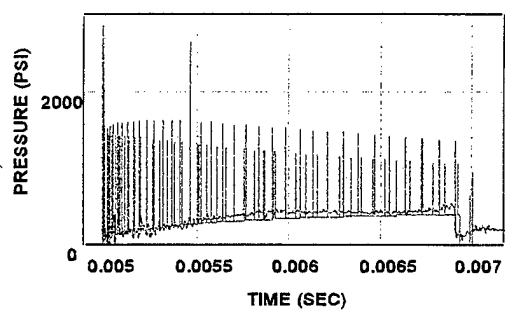


PRESSURE-TIME CURVES

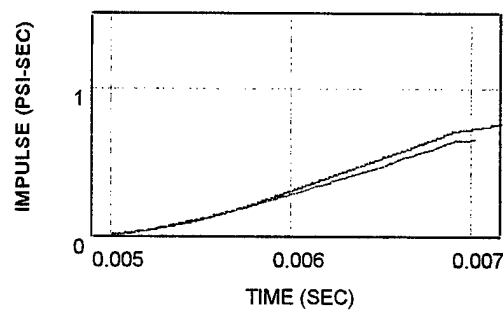


IMPULSE-TIME CURVES

a. Gage A, 12-Foot Standoff, 2-Inch Height

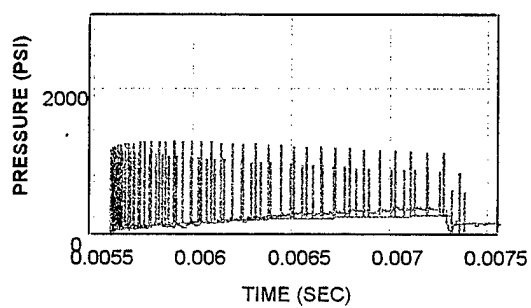


PRESSURE-TIME CURVES

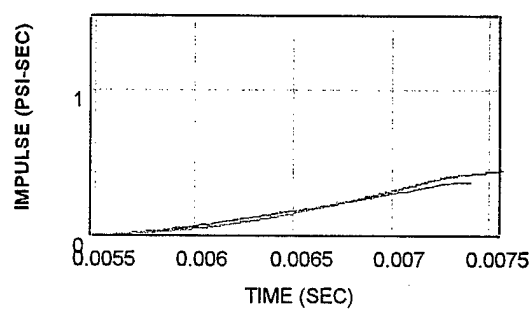


IMPULSE-TIME CURVES

b. Gage B, 15-Foot Standoff, 2-Inch Height



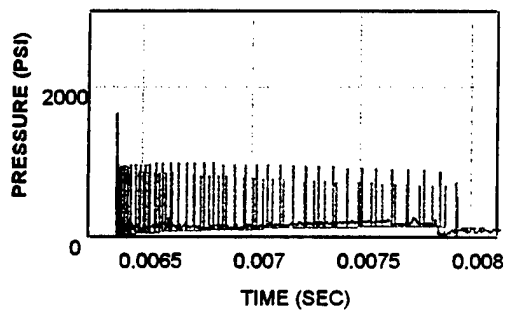
PRESSURE-TIME CURVES



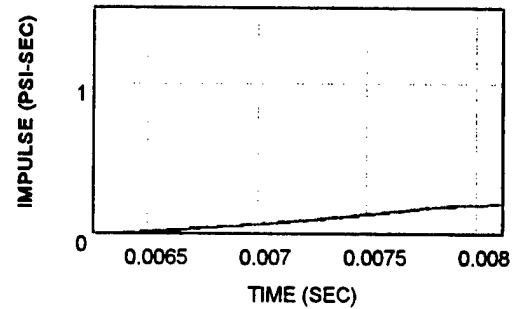
IMPULSE-TIME CURVES

c. Gage C, 18-Foot Standoff, 2-Inch Height

Figure A-4. Results for M58 Shot 4286 with Variable ϕ

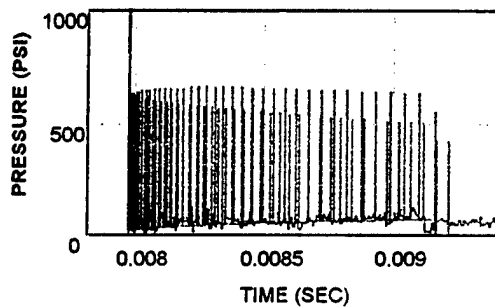


PRESSURE-TIME CURVES

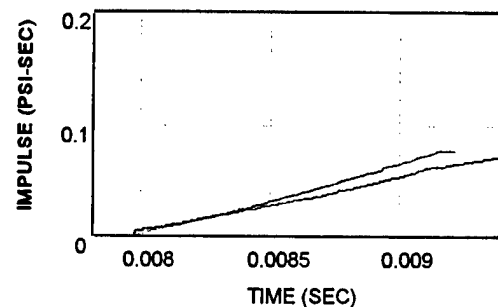


IMPULSE-TIME CURVES

d. Gage E, 22-Foot Standoff, 2-Inch Height

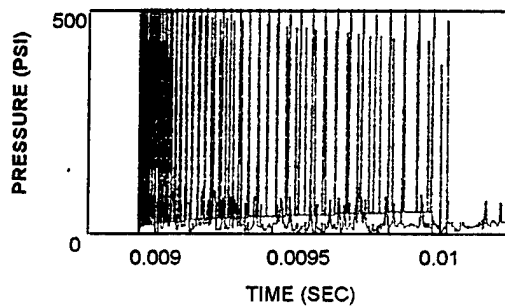


PRESSURE-TIME CURVES

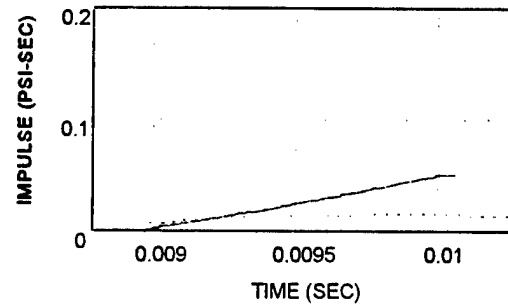


IMPULSE-TIME CURVES

e. Gage H, 30-Foot Standoff, 2-Inch Height



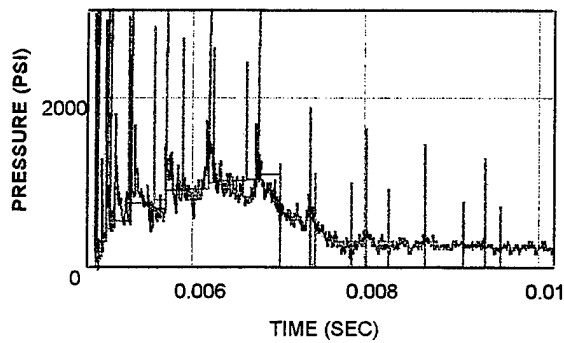
PRESSURE-TIME CURVES



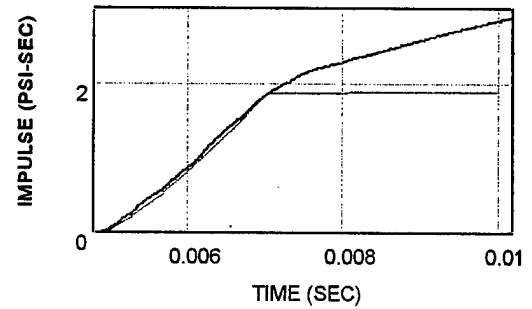
IMPULSE-TIME CURVES

f. Gage J, 35-Foot Standoff, 2-Inch Height

Figure A-4. Results for M58 Shot 4286 with Variable ϕ (Continued)

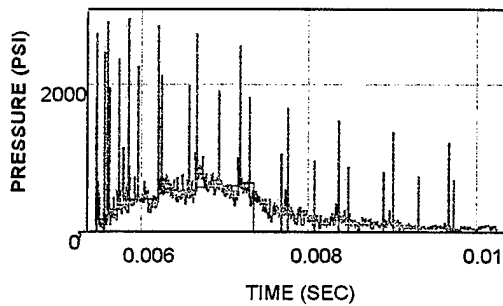


PRESSURE-TIME CURVES

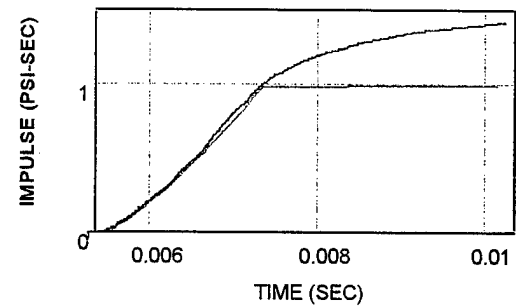


IMPULSE-TIME CURVES

a. Gage A, 12-Foot Standoff, 2-Inch Height

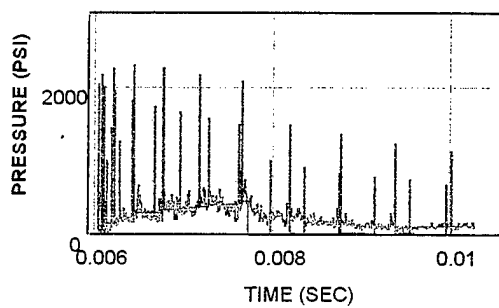


PRESSURE-TIME CURVES

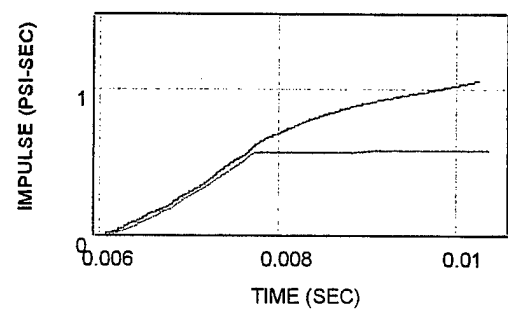


IMPULSE-TIME CURVES

b. Gage B, 15-Foot Standoff, 2-Inch Height



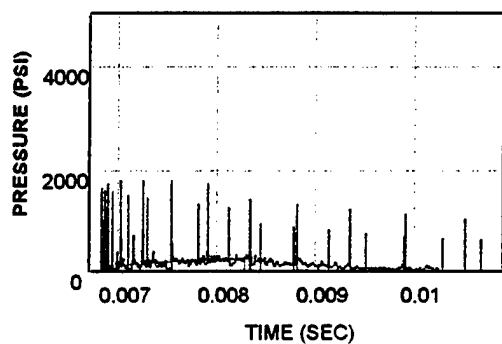
PRESSURE-TIME CURVES



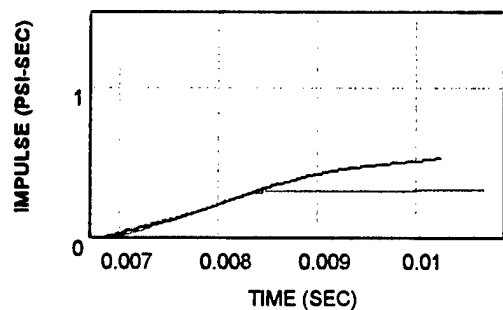
IMPULSE-TIME CURVES

c. Gage C, 18-Foot Standoff, 2-Inch Height

Figure A-5. Results for D-Sabre Shot 4287 with Variable ϕ

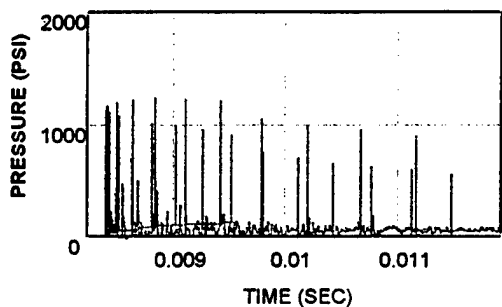


PRESSURE-TIME CURVES

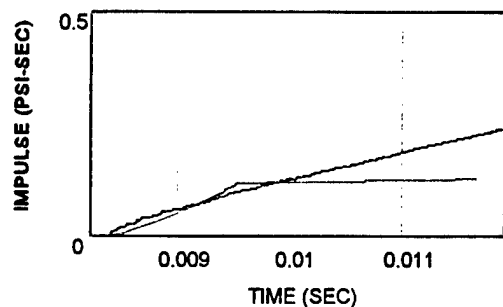


IMPULSE-TIME CURVES

d. Gage E, 22-Foot Standoff, 2-Inch Height

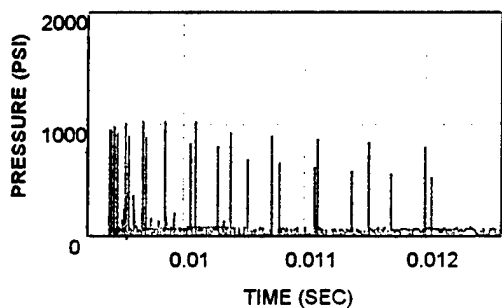


PRESSURE-TIME CURVES

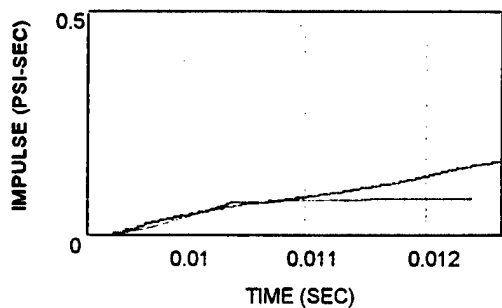


IMPULSE-TIME CURVES

e. Gage H, 30-Foot Standoff, 2-Inch Height



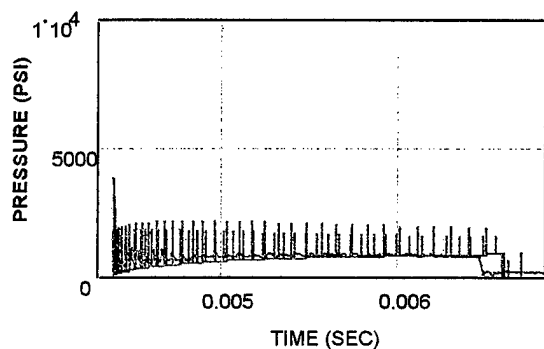
PRESSURE-TIME CURVES



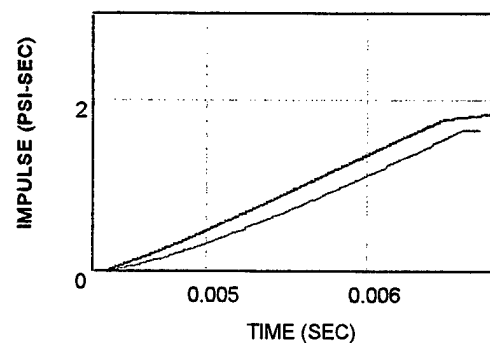
IMPULSE-TIME CURVES

f. Gage J, 35-Foot Standoff, 2-Inch Height

Figure A-5. Results for D-Sabre Shot 4287 with Variable ϕ (Continued)

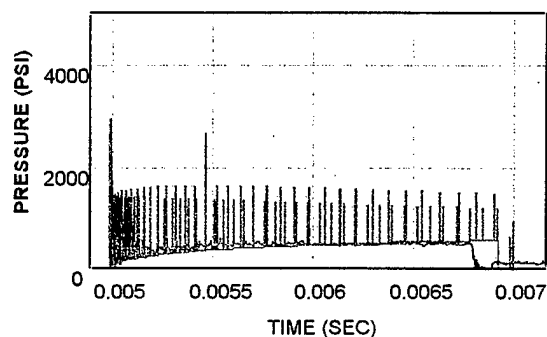


PRESSURE-TIME CURVES

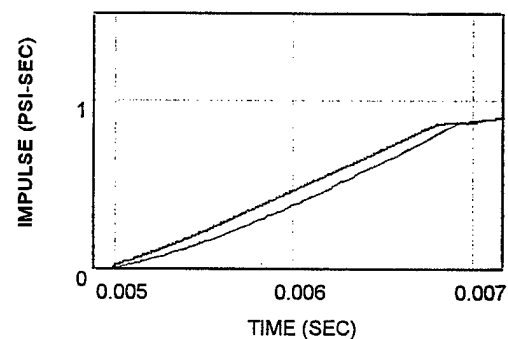


IMPULSE-TIME CURVES

a. Gage A, 12-Foot Standoff, 2-Inch Height

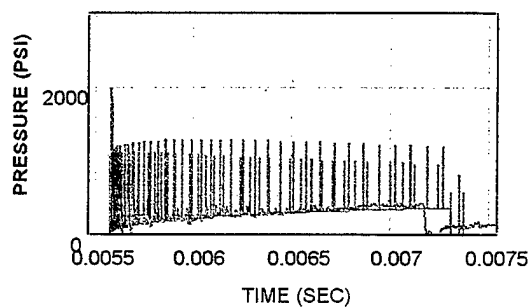


PRESSURE-TIME CURVES

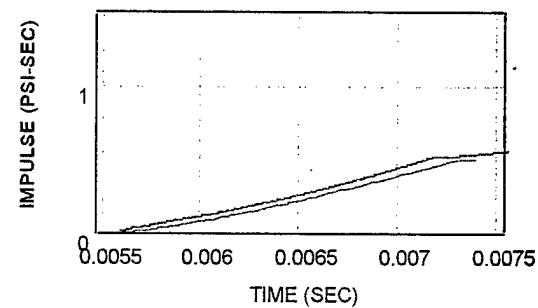


IMPULSE-TIME CURVES

b. Gage B, 15-Foot Standoff, 2-Inch Height



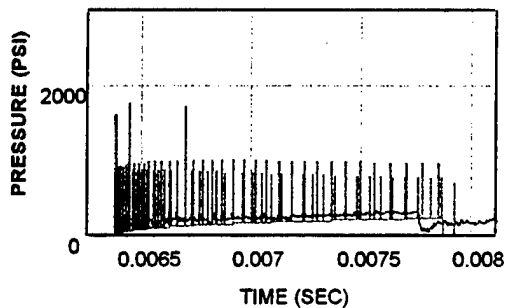
PRESSURE-TIME CURVES



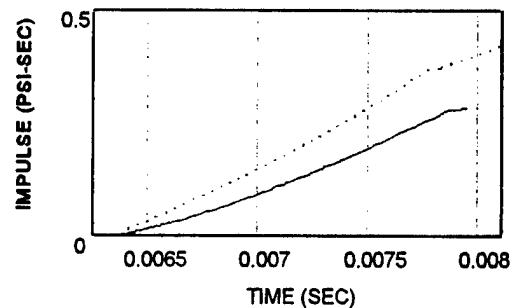
IMPULSE-TIME CURVES

c. Gage C, 18-Foot Standoff, 2-Inch Height

Figure A-6. Results for C-Sabre Shot 4288 with Variable ϕ

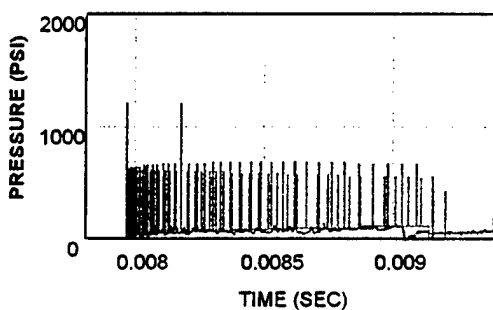


PRESSURE-TIME CURVES

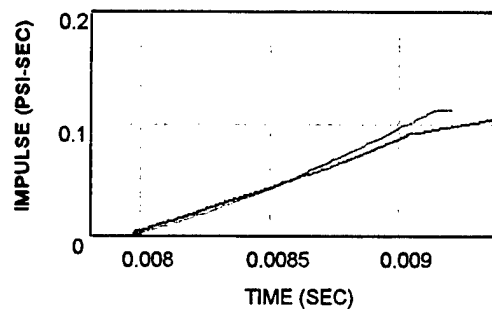


IMPULSE-TIME CURVES

d. Gage E, 22-Foot Standoff, 2-Inch Height

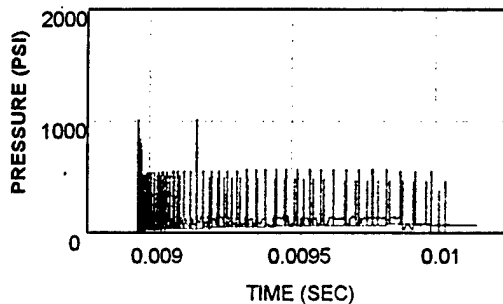


PRESSURE-TIME CURVES

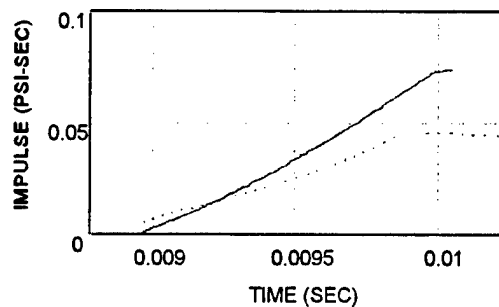


IMPULSE-TIME CURVES

e. Gage H, 30-Foot Standoff, 2-Inch Height



PRESSURE-TIME CURVES



IMPULSE-TIME CURVES

f. Gage J, 35-Foot Standoff, 2-Inch Height

Figure A-6. Results for C-Sabre Shot 4288 with Variable ϕ (Continued)

DISTRIBUTION

ADMINISTRATOR DEFENSE TECH INFO CTR ATTN DTIC-OCF 8725 JOHN J KINGMAN RD STE 0944 FT BELVOIR VA 22060-6218	1	OFFICE OF NAVAL RESEARCH BALLSTON TOWER 1 ATTN 321 (D TODEROFF) 800 NORTH QUINCY STREET ARLINGTON VA 22217-5660	1
JHU/CPIA ATTN SECURITY OFFICER 10630 LITTLE PATUXENT PKWY STE 202 COLUMBIA MD 21044-3200	1	OFFICE OF NAVAL RESEARCH BALLSTON TOWER 1 ATTN 321 (T SWEAN) 800 NORTH QUINCY STREET ARLINGTON VA 22217-5660	1
CENTER FOR NAVAL ANALYSES 4401 FORD AVENUE ALEXANDRIA VA 22302-0268	1	NAVAL RESEARCH LABORATORY ATTN TECHNICAL LIBRARY 4555 OVERLOOK DR SW WASHINGTON DC 20375-5320	1
OFFICE OF NAVAL RESEARCH BALLSTON TOWER 1 ATTN 33 (S LEKODIS) 800 NORTH QUINCY STREET ARLINGTON VA 22217-5660	1	NAVAL RESEARCH LABORATORY ATTN 6440 (M EMERY) 4555 OVERLOOK DR SW WASHINGTON DC 20375-5320	1
OFFICE OF NAVAL RESEARCH BALLSTON TOWER 1 ATTN 333 (J FEIN) 800 NORTH QUINCY STREET ARLINGTON VA 22217-5660	1	NAVAL RESEARCH LABORATORY ATTN 7131 (W SZYMCZAK) 4555 OVERLOOK DR SW WASHINGTON DC 20375-5320	1
OFFICE OF NAVAL RESEARCH BALLSTON TOWER 1 ATTN 333 (J GOLDWASSER) 800 NORTH QUINCY STREET ARLINGTON VA 22217-5660	1	SUPERINTENDENT NAVAL POSTGRADUATE SCHOOL ATTN TECHNICAL LIBRARY MONTEREY CA 93940	1
OFFICE OF NAVAL RESEARCH BALLSTON TOWER 1 ATTN 4524 (J GAGORIK) 800 NORTH QUINCY STREET ARLINGTON VA 22217-5660	1	SUPERINTENDENT NAVAL POSTGRADUATE SCHOOL ATTN 69SG (Y SHIN) MONTEREY CA 93940	1
OFFICE OF NAVAL RESEARCH BALLSTON TOWER 1 ATTN 321 (D HAN) 800 NORTH QUINCY STREET ARLINGTON VA 22217-5660	1	DIRECTOR DEFENSE SPECIAL WEAPONS AGENCY ATTN TECHNICAL LIBRARY 6801 TELEGRAPH RD ALEXANDRIA VA 22310-3398	1

DIRECTOR DEFENSE SPECIAL WEAPONS AGENCY ATTN SPSD (K GOERING) 6801 TELEGRAPH RD ALEXANDRIA VA 22310-3398	1	COMMANDING OFFICER COASTAL SYS STA DAHLGREN DIVISION NSWC ATTN LIBRARY 6730 W HWY 98 PANAMA CITY FL 32407-7001	1
DIRECTOR DEFENSE SPECIAL WEAPONS AGENCY ATTN SPSD (D BRUDER) 6801 TELEGRAPH RD ALEXANDRIA VA 22310-3398	1	COMMANDER NAVAL SEA SYSTEMS COMMAND ATTN PMS407 2561 JEFFERSON DAVIS HIGHWAY ARLINGTON VA 22242-5160	1
DIRECTOR DEFENSE SPECIAL WEAPONS AGENCY ATTN SPSD (M GILTRUD) 6801 TELEGRAPH RD ALEXANDRIA VA 22310-3398	1	LIBRARY OF CONGRESS ATTN GIFT AND EXCHANGE WASHINGTON DC 20540	1
DIRECTOR DEFENSE SPECIAL WEAPONS AGENCY ATTN SPWE (E TREMBA) 6801 TELEGRAPH RD ALEXANDRIA VA 22310-3398	1	LOS ALAMOS NATIONAL LABORATORY ATTN TECHNICAL LIBRARY PO BOX 1663 LOS ALAMOS NM 87545	1
COMMANDING OFFICER COASTAL SYS STA DAHLGREN DIVISION NSWC ATTN 10C (D CRUTE) 6730 W HWY 98 PANAMA CITY FL 32407-7001	1	LOS ALAMOS NATIONAL LABORATORY ATTN F668 (J REPA) PO BOX 1663 LOS ALAMOS NM 87545	1
COMMANDING OFFICER COASTAL SYS STA DAHLGREN DIVISION NSWC ATTN 10C (D ROBESON) 6730 W HWY 98 PANAMA CITY FL 32407-7001	1	LOS ALAMOS NATIONAL LABORATORY ATTN EES5 (T DEY) PO BOX 1663 LOS ALAMOS NM 87545	1
COMMANDING OFFICER COASTAL SYS STA DAHLGREN DIVISION NSWC ATTN 043 (J ALLEN) 6730 W HWY 98 PANAMA CITY FL 32407-7001	1	LOS ALAMOS NATIONAL LABORATORY ATTN EES5 (R P SWIFT) PO BOX 1663 LOS ALAMOS NM 87545	1
		MECHANICAL ENGINEERING JOHNS HOPKINS UNIVERSITY ATTN A PROSPERETTI BALTIMORE MD 21218	1
		DYNAFLOW INC ATTN G L CHAHINE 7210 PINDELL SCHOOL RD FULTON MD 20759	1

DYNAFLOW INC		Internal:	
ATTN R DURAISWAMI		PM3 (R KAVETSKY)	1
7210 PINDELL SCHOOL RD		IS	1
FULTON MD 20759	1	40 (W HINCKLEY)	1
		40E (E JOHNSON)	1
SRI INTERNATIONAL		40P2 (BURCK)	1
ATTN P GEFKEN		40P4 (L TAYLOR)	1
333 RAVENSWOOD AVE		40P7 (M KAREN)	1
MENLO PARK CA 94025-3434	1	410	1
		4130 (P ONG)	1
SRI INTERNATIONAL		4140 (R GARRETT)	1
ATTN M SANAI		420 (B ALMQUIST)	1
333 RAVENSWOOD AVE		420 (R McKEOWN)	1
MENLO PARK C 94025-3434	1	420C2 (J RENZI)	1
		4210 (D TAM)	1
ATR		4210 (A DARE)	1
ATTN C SMITH		4210 (B GODZUK)	1
15210 DINO DRIVE		4210 (T YOUNG)	1
BURTONSVILLE MD 20866	1	4220 (J BURNS)	1
		4220 (D MARUSZEWSKI)	1
ATR		4220 (D NELL)	1
ATTN J GOELLER		4230 (A WARDLAW)	1
15210 DINO DRIVE		4230 (A LUTON)	1
BURTONSVILLE MD 20866	1	450D3 (L LIPTON)	1
		4610 (R THRUN)	1
SAIC		4620 (K KIDDY)	1
ATTN R BRITT		4620 (J KOENIG)	1
PO BOX 469		4620 (W McDONALD)	10
ST JOSEPH LA 71366-0469	1	4630 (R BENDT)	1
		4630 (J GASPIN)	1
SAIC		4630 (F HAINS)	1
ATTN MS C2 (R ALLEN)		4630 (G HARRIS)	1
10260 CAMPUS POINT DR		56D (O'DONNELL)	1
SAN DIEGO CA 92121-1570	1	590 (TSE)	1
		630 (FALKLER)	1
ROYAL SYSTEMS		6310A (SHERLOCK)	1
ATTN O DENGEL		6310R (ROSS)	1
6294 BROWNTOWN RD		840L	3
FRONT ROYAL VA 22630	1	8430	1
		9210 (R GUIRGUIS)	1
D E PHILLIPS ASSOCIATES			
ATTN D PHILLIPS			
PO BOX 671			
MIDDLETOWN MD 21769-0671	1		